2016

Improving Efficiency of Thermoelectric Devices Made of Si-Ge, Si-Sn, Ge-Sn, and Si-Ge-Sn Binary and Ternary Alloys

SEYEDEH NAZANIN KHATAMI
University of Massachusetts Amherst

IMPROVING EFFICIENCY OF THERMOELECTRIC DEVICES MADE OF SI-GE, SI-SN, GE-SN AND SI-GE-SN BINARY AND TERNARY ALLOYS

A Thesis Presented

by

SEYEDEH NAZANIN KHATAMI

Submitted to the Graduate School of the
University of Massachusetts Amherst in partial fulfillment
of the requirements for the degree of

MASTER OF SCIENCE IN ELECTRICAL AND COMPUTER ENGINEERING

2016 September

Electrical and Computer Engineering

IMPROVING EFFICIENCY OF THERMOELECTRIC DEVICES MADE OF SI-GE, SI-SN, GE-SN AND SI-GE-SN BINARY AND TERNARY ALLOYS

A Thesis Presented

by

SEYEDEH NAZANIN KHATAMI

Approved as to style and content by:

Zlatan Aksamija, Chair

Neal G. Anderson, Member

Eric Polizzi, Member

Christopher V. Hollot, Department Head
Electrical and Computer Engineering

DEDICATION

I dedicate this work with special feeling of gratitude to my parents, Seyed Ezzat and Sholeh, and my husband, Arman. I am truly thankful for having you in my life.

ACKNOWLEDGMENTS

I am so grateful to have performed my graduate studies at University of Massachusetts Amherst, department of electrical and computer engineering. I would like to thank my advisor, Prof. Zlatan Aksamija, for his unlimited help and supports through this process. Special thanks to Prof. Neal Anderson and Prof. Eric Polizzi, for kindly serving as my thesis committee members and providing valuable suggestions.

ABSTRACT

IMPROVING EFFICIENCY OF THERMOELECTRIC DEVICES MADE OF SI-GE, SI-SN, GE-SN AND SI-GE-SN BINARY AND TERNARY ALLOYS

2016 SEPTEMBER

SEYEDEH NAZANIN KHATAMI

B.Tech., WESTERN NEW ENGLAND UNIVERSITY

M.S.E.C.E., UNIVERSITY OF MASSACHUSETTS AMHERST

Directed by: Professor Zlatan Aksamija

Thermoelectric devices with the ability to convert rejected heat into electricity are widely used in nowadays technology. Several studies have been done to improve the efficiency of these devices. However, because of the strong correlation between thermoelectric properties (electrical conductivity, Seebeck coefficient, and thermal conductivity including lattice and electron counterpart), improving ZT has always been a challenging task. In this study, thermal conductivity of group IV-based binary and ternary alloys such as SiGe, SiSn, GeSn, and SiGeSn has been studied. Phonon Boltzmann Transport Equation has been solved in the relaxation time approximation including intrinsic and extrinsic (in the presence of boundary and interfaces in the low-dimensional material) scattering mechanisms. Full phonon dispersion based on the Adiabatic Bond Charge model has been calculated for Si, Ge, and Sn. Virtual crystal approximation has been adapted to calculate the dispersion of SiGe, SiSn,

GeSn, and SiGeSn. Two approaches have been introduced to reduce the lattice thermal conductivity of the materials under study. First, alloying results in a significant reduction of thermal conductivity. But, this reduction has been limited by the mass disorder scattering in the composition range of 0.2 to 0.8. Second, nanostructuring technique has been proposed to further reduce the thermal conductivity. Our study shows that, due to the atomic mass difference which gives rise to the elastic mass scattering mechanism, SiSn has the lowest thermal conductivity among the other materials under study. SiSn achieved the thermal conductivity of 1.18 W/mK at 10 nm at the Sn composition of 0.18, which is the experimentally stable state of SiSn. The results show that SiSn alloys have the lowest conductivity (3 W/mK) of all the bulk alloys, more than two times lower than SiGe, attributed to the larger difference in mass between the two constituents. In addition, this study demonstrates that thin films offer an additional reduction in thermal conductivity, reaching around 1 W/mK in 20 nm SiSn, GeSn, and ternary SiGeSn films, which is close to the conductivity of amorphous SiO_2. This value is lower than the thermal conductivity of SiGe at 10 nm which is 1.43 W/mK. Having lattice thermal conductivity reduced, electron transport has been studied by solving Boltzmann Transport Equation under low electric field including elastic and inelastic scattering mechanisms. Rode's iterative method has been applied to the model for obtaining perturbation of distribution function under low electric field. This study shows that nanostructuring and alloying can reduce κ_{ph} without significantly changing the other parameters. This is because of the phonon characteristics in solids in which MFP of phonons is much larger than those of electrons, which gives us the possibility of phonons confinement without altering electrons transport. Thermoelectric properties of SiGe in the bulk and nanostructure form have been studied to calculate ZT in a wide range of temperatures. The results demonstrate that ZT reaches the value of 1.9 and 1.58 at the temperatures of 1200 K and 1000 K respectively, with the Ge composition of 0.2 and carrier concentration of

5×10^{19} cm^{-3} at 10 nm thickness. This model can be applied to SiSn and other binary and ternary alloys, to calculate the improved ZT. Hence, we conclude that group IV alloys containing Sn have the potential for high-efficiency TE energy conversion.

TABLE OF CONTENTS

LIST OF FIGURES

Figure **Page**

CHAPTER 1

INTRODUCTION

1.1 Overview

Energy crisis, climate and environmental issues as well as global demand for sustainable and renewable energy have made alternative sources of energy very attractive. Based on Lawrence Livermore National Laboratory data on 2015, 59.4 quads of energy is rejected annually in the US alone. Efficient thermoelectric (TE) devices are needed to recover the huge amount of waste heat that can be used as a source of energy. Thermoelectric devices were first proposed on 1821 and consequently Seebeck, Peltier and Thompson effects were established thereafter. Thermo-electric devices which are solid states heat engines, have the ability of converting heat directly into electricity from temperature gradients. There are many applications attributed to them, such as coal and solar power plant and combustion engine. Based on the direction of energy conversion, Peltier effect or Seebeck effect may occur. Thermoelectric devices are based on the coupling process between heat and charge transport in many materials and have increasing potential for practical application. They are reliable devices with long life-time durability. However, the most critical disadvantage of TE devices are their low efficiency and cost which have limited their applicability. Hence, these devices have instigated tremendous research attention. Heat and charge transport in materials are coupled processes that lead to thermoelectric effects such as changes in the temperature gradient that results in a voltage drop, and vice versa. Thermoelectric effects have practical applications to refrigeration and power generation. In order to harvest thermal energy from any sources (i.e. car exhaust, CPU

of a computer,...) efficient thermoelectric devices are needed. Hence wherever waste heat exists, thermoelectric devices can be applied. Unfortunately the efficiency of thermoelectric devices is not at a satisfactory level to meet the demand of current technologies. However, there have been continuous efforts in improving efficiency of thermoelectric devices in recent decades. Thermoelectric efficiency is defined as the ratio of heat absorbed over the energy produced, as seen below:

$$\eta = \left(1 - \frac{T_C}{T_H}\right)\left(\frac{\sqrt{Z\overline{T}+1}-1}{\sqrt{Z\overline{T}+1}+\frac{T_C}{T_H}}\right), \tag{1.1}$$

In the equation above $1 - \frac{T_C}{T_H}$ is the Carnot limit (The maximum efficiency of the devices that theoretically can be achieved) which is limited by ZT. T_C is temperature on the cold side and T_H is the temperature of the hot reservoir between which the temperature gradient is applied and the resulting heat flux is maintained. Figure of merit (ZT) which strongly governs thermoelectric efficiency is defined by a dimensionless expression [17]

$$ZT = \frac{S^2\sigma T}{\kappa_l + \kappa_e}, \tag{1.2}$$

where S is the Seebeck coefficient, σ is the electrical conductivity ($S^2\sigma$ is called the power factor), T is the absolute temperature, and κ is the total thermal conductivity including both the carrier and phonon counterparts. Typically, the lattice (phonon) contribution dominates over the electronic counterpart, in other words heat conduction in semiconductors is dominated by phonon transport [4]. In order to increase the efficiency of TE materials, one can increase the numerator and/or decrease the denominator of ZT. In essence to improve efficiency, one can decrease the thermal conductivity while boosting the ZT. In the first part of this study, decreasing thermal conductivity of the material is our primary goal.

1.2 Thermoelectric Devices Based on the Semiconductors

There is an interdependence between the parameters in ZT. This interdependence compromise between the Seebeck coefficient, electrical conductivity and thermal conductivity, and must be considered to maximize thermoelectric figure of merit. Typically, ZT peaks at carrier concentrations between 10^{19} and 10^{21} carriers per cm^{-3} which can be achieved in heavily doped semiconductors [50]. Insulators have a low figure of merit due to their small electrical conductivities. In metals, heat and charge transport are coupled processes. They have high electrical conductivities with large thermal conductivities and low Seebeck coefficients leading to a very low ZT. However, in semiconductors heat and charge are largely decoupled. Power factor ($S^2\sigma$) is governed by charge carrier transport which can be manipulated by doping. In addition, thermal conductivity is under the control of phonon scattering, this implies that the lattice thermal conductivity can be reduced without significantly affecting the electrical conductivity [5]. Most moderately doped semiconductors have high electrical conductivity and a moderate Seebeck coefficient. However, ZT is still limited in bulk form due to high thermal conductivity mostly dominated by the phonon contribution. Hence κ_{el} can be tuned to some extent, without adversely affecting the power factor. Due to the interdependence of material properties, it has been challenging to increase $ZT > 1$ with bulk materials. However, a ZT of 1.5-2 may be sufficient for some applications such as vehicle heat recovery, car cooling/heating, and home co-generation [59]. Several studies demonstrate $ZT > 1$ based on some form of nanostructuring, however the goal of $ZT > 3$ has not yet been achieved [58]. Silicon (Si) is considered to be the basis of modern electronics. This makes it a relatively inexpensive and abundant semiconductor, especially when comparing it to other popular room-temperature thermoelectric materials, such as bismuth telluride (Bi_2Te_3), which has a low thermal conductivity [7]. On the other hand, Si, as a bulk material, is not a very efficient thermoelectric material due to its low conversion efficiency

[6]. Its efficiency is limited primarily by a large lattice contribution to the thermal conductivity of 146 W/mK [23, 35] at room temperature, which limits the ZT to approximately 0.05 [31]. Similar arguments apply to other bulk group IV material such as germanium (Ge). The cost effectiveness as well as the demand for improving efficiency of group IV materials, including Si, Ge, and Sn, provoked us to focus our study on the combination of these materials.

1.3 Approaches

In this study, we have proposed to improve the overall thermoelectric efficiency of binary and ternary group IV alloys such as SiGe, SiSn, GeSn, and SiGeSn materials. In order to achieve this goal, we have proposed two approaches- alloying and nanostructuring. Alloying is the first approach we have applied. This method has been successful in improving the thermoelectric conversion efficiency of many bulk materials, including Si and Ge [10]. The SiGe alloy has typically been used for TE conversion at high temperatures having $ZT > 1$ around $900K$ [49]. The improvement in ZT of bulk alloys is mostly due to the reduction of lattice thermal conductivity κ_{ph}. This reduction arises from large increases in phonon scattering due to random mass variation. However, this reduction is limited by alloying alone which will be further explained in the Section 3.1. Hence, additional methods of reducing the lattice thermal conductivity in alloys are highly desirable.

Another approach to improve TE conversion efficiency is using low-dimensional nanostructures [18, 24]. This approach was first proposed theoretically by Hicks and Dresselhaus in 1993 [25]. Decreasing the size below the mean free (MFP) path in the bulk materials results in two benefits. First and foremost, a significant decrease in the thermal conductivity, which is our goal for improving thermoelectric conversion efficiency [26, 37, 63]. The second is an increase in the power factor due to the reduction in the dimensionality [47]. Nevertheless, reducing lattice thermal conductivity

without significantly affecting the Seebeck coefficient or electrical conductivity is a way to increase the overall ZT which is the main focus in the first part of this study.

The remainder of this thesis document will discuss how applying these approaches (alloying and nanostructuring) result in reduction of thermal conductivity. In chapter 2, we show the phonon dispersion of the materials under study. In chapter 3, we discuss phonon transport in bulk and nanostructures including intrinsic and extrinsic scattering mechanisms and the corresponding results is provided in chapter 4. The electron transport is discussed in chapter 5. The electronic calculation and results are demonstrated in chapter 6.1. And finally in chapter 6.2 we include the result of improved ZT.

CHAPTER 2

PHONON DISPERSION

Regular arrangement of atoms in the crystal is called a lattice, which is formed due to the constant spacing between the atoms. Si, Ge, and α-Sn, semiconductors of the group IV have face centered cubic (fcc) structure. As atoms in the crystal gain energy, they vibrate around their equilibrium position. Due to these lattice vibrations, the crystal is able to store energy. These lattice vibrations are called phonons and they are thermal energy transmitters. Phonons are considered as thermal energy in the form of heat. Hence, the study of phonons plays an important role in both thermal and electrical conductivity. Phonons have harmonic vibrations similar to the vibrations of a mass and spring. Thus, their vibration can be modeled as solids including the collection of mass that are connected through springs. Therefore, their acceleration is the second derivative of displacement. As a result phonon dispersion, which is the vibrational frequency of phonons as a function of wave vectors, can be obtained. Group velocity, one of the important characteristics that will be needed in calculating the thermal conductivity, is obtained from dispersion. Group velocity is the derivative of frequency with respect to wave vector. In a 3D crystal it is obtained from the gradient of frequency in three directions x, y, and z.

$$\vec{v_g}(\vec{k}) = \left[\frac{\partial \omega(\vec{k})}{\partial k_x}, \frac{\partial \omega(\vec{k})}{\partial k_y}, \frac{\partial \omega(\vec{k})}{\partial k_z} \right], \tag{2.1}$$

where ω is the frequency, k is the wave vector in three directions x, y, and z. Atoms in 3D structure of a crystal are allowed to move in three directions relative to the

direction of lattice wave propagation. If the direction of the atom displacement is parallel to the direction of propagation, longitudinal waves are produced. And if the direction of the atom displacement is perpendicular to the direction of propagation, transverse waves are made. In this study, calculating the phonon dispersion of SiGe, SiSn, GeSn, and SiGeSn is required to obtain the characteristics needed from their dispersion relation. Full phonon dispersion based on Weber's adiabatic bond charge (ABC) model [61] can be calculated. The ABC model includes interactions between ions, bond charges, bond bending, and long-range electrostatic interactions, and has been shown to reproduce measured phonon vibrational frequencies in virtually all group IV [4, 34, 46, 61], III-V [46, 53], and II-VI [42] semiconductors with excellent accuracy. The ABC phonon dispersions for Si can be found in Refs. [4, 61], and for Ge in Refs. [46, 61]. Vibrational properties of $Si_{1-x}Ge_xSn_y$ alloys, including phonon dispersion and velocity, are calculated here in the virtual crystal approximation (VCA) [1]. Dispersion of tin has been calculated based on the adiabatic bond charge model, shown in Fig. 2.1. The experimental data from Ref. [41] matched with the numerical simulation results obtained in this study. α-Sn with atomic mass of 118.71 amu has higher atomic mass and therefore larger density in comparison with Si and Ge with atomic mass of 28.0855 amu and 72.640 amu respectively. This results in lower vibrational frequency in the dispersion curve and consequently lower phonon group velocity. As a result of a lower phonon group velocity and heavier mass, a decrease in thermal conductivity of tin-based alloys is expected. Dispersion relation of α-Sn is lower in comparison with Si and Ge due to higher atomic mass of Sn. The dispersion of α-Sn inspired us that making alloy of group IV semiconductors including α-Sn, can reduce thermal conductivity further than SiGe which has been studied comprehensively for TE applications. In the Fig. 2.1 dispersion of $Ge_{0.5}Sn_{0.5}$ (dotted lines) $Si_{0.5}Sn_{0.5}$ (dashed lines), which has been calculated using VCA method, along

with the dispersion of pure Sn are shown. The symbols represent the experimental measurement of pure α-Sn from [41].

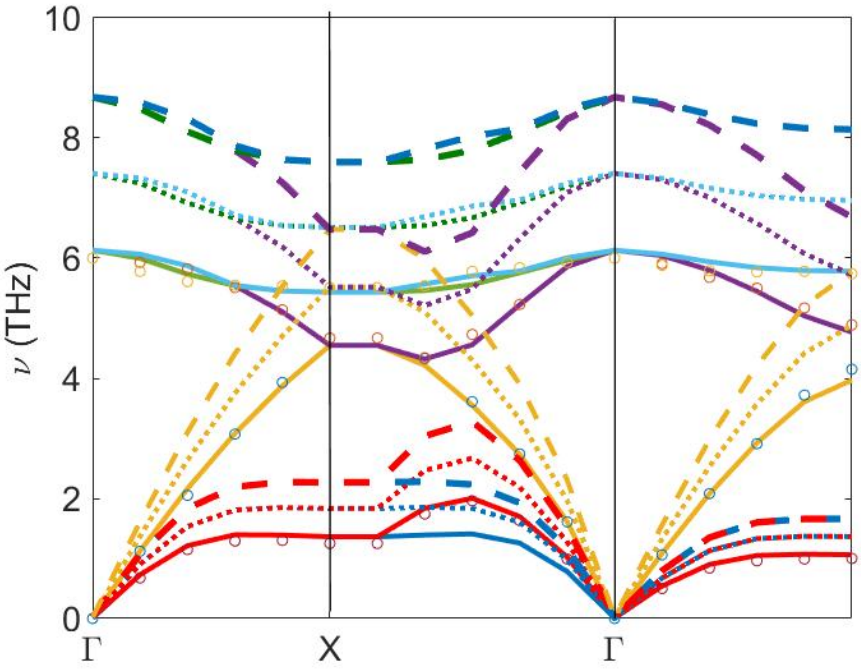

Figure 2.1. Phonon dispersion curves for α-Sn, $Si_{0.5}Sn_{0.5}$ and $Ge_{0.5}Sn_{0.5}$ showing the vibrational frequencies (THz) vs. the phonon wave vector. The symbols represent experimental measurement of α-Sn from [41] and solid lines are the numerical simulation of α-Sn. Dotted lines represent the dispersion of $Ge_{0.5}Sn_{0.5}$ and dashed lines depicts the dispersion of $Si_{0.5}Sn_{0.5}$ [27].

.

CHAPTER 3

PHONON TRANSPORT

3.1 Boltzmann Transport Equation

Macroscale rate of heat transfer is explained by the Fourier's law as:

$$\vec{q} = \kappa \nabla T, \tag{3.1}$$

where $\vec{q}$ is the heat flux, κ is the thermal conductivity and ∇T is the temperature gradient. In the nanoscale, Fouriers law of heat conduction becomes less accurate as the size of the system becomes significantly smaller than the MFP. The MFP is the average distance the phonon travels before scattering [30]. Hence understanding the process of going from micro-scale down to nanoscale in electron and phonon transport is crucial. Most semi-classical theories of transport in solids for either electrons and/or phonons employ the Boltzmann transport equation (BTE). Applying a temperature gradient, distribution function of phonons and electrons can be obtained by solving the BTE. In the complete 3D time-dependent form, the BTE requires time, space and momentum variables. In device simulation, one of the most convenient approaches is to solve BTE in relaxation time approximation (RTA) by separating the symmetric and asymmetric sections. This approximation is validated in the case that elastic scattering is dominant. The steady state distribution function can be calculated by solving the time independent BTE in the RTA. In this part of the study, BTE is solved for phonon transport including the intrinsic and extrinsic scattering rates. For

a distribution function $N_{b,q}(x,y,z)$ which is a small deviation from the equilibrium state $N^0_{b,q}$, the phonon BTE (pBTE) is given by [13]:

$$\vec{v}_{\mathrm{b},\vec{q}} \cdot \vec{\nabla} N_{\mathrm{b},\vec{q}}(x,y,z) = -\frac{N_{\mathrm{b},\vec{q}}(x,y,z) - N^0_{\mathrm{b},\vec{q}}(T)}{\tau^{int}_{\mathrm{b}}(\vec{q})}. \tag{3.2}$$

As indicated in the pBTE, the steady-state phonon distribution function $N_{b,q}(x,y,z)$ is a function of the phonon branch b, wave vector q and position in 3D space (x,y,z). τ^{int}_q is the relaxation time due to all of the intrinsic scattering mechanisms including both resistive umklapp and non-resistive normal anharmonic phonon-phonon, isotope, impurity, and alloy mass difference interactions. τ^{int}_q can be obtained using the standard single-mode relaxation time approximation [38]. The equations hold for each branch, and inter-branch scattering which is included in $\tau^{int}_{\mathrm{b}}(\vec{q})$. In the calculation of relaxation time $\tau^{int}_{\mathrm{b}}(\vec{q})$ for a phonon in mode b and with wave vector $\vec{q}$, we consider normal $\tau_{\mathrm{b,N}}(\vec{q})$ and umklapp $\tau_{\mathrm{b,U}}(\vec{q})$ three-phonon scattering, impurity $\tau_{\mathrm{b,I}}(\vec{q})$, and mass-disorder $\tau_{\mathrm{b,Mass}}(\vec{q})$ scattering. The total intrinsic relaxation time is given by:

$$\frac{1}{\tau^{int}_{\mathrm{b}}(\vec{q})} = \frac{1}{\tau_{\mathrm{b,N}}(\vec{q})} + \frac{1}{\tau_{\mathrm{b,U}}(\vec{q})} + \frac{1}{\tau_{\mathrm{b,I}}(\vec{q})} + \frac{1}{\tau_{\mathrm{b,Mass}}(\vec{q})}. \tag{3.3}$$

3.1.1 Mass Scattering

The combination of $Si_{1-x-y}Ge_xSn_y$, results in variation in the local atomic mass that leads to strong mass-difference scattering of phonons. In the case of alloys, mass-difference disorder will have three components: alloying, isotopic mass variation, and the small local strain field induced by variations in the atomic species (Si, Ge or Sn). The scattering strength will be proportional to the total fraction of mass-disordered constituents [13]:

$$\Gamma_{\mathrm{Mass}}(x) = \Gamma_{\mathrm{Alloy}}(x) + \Gamma_{\mathrm{Iso}}(x) + \Gamma_{\mathrm{Strain}}(x). \tag{3.4}$$

The mass-difference constant is defined as [2]:

$$\Gamma_{\text{Alloy}} = \sum_i f_i (1 - M_i/\bar{M})^2, \tag{3.5}$$

where f_i is the proportion of material i with mass M_i, while the average mass is $\bar{M} = \sum_i f_i M_i$ [38].

The primary driver of thermal conductivity reduction from pure Si, Ge or Sn to the SiGe, SiSn or GeSn alloy is the quadratic dependence on the germanium concentration in alloy mass-difference. The energy dependence of the alloy scattering rate follows a Rayleigh-like ($\tau^{-1} \propto \omega^4$) trend and is calculated from the vibrational density of states as [54, 33]:

$$\frac{1}{\tau_{\text{Mass}}(\omega)} = \frac{\pi}{6} V_0 \Gamma_{\text{Mass}} \omega^2 \, D(\omega), \tag{3.6}$$

where V_0 is the volume per atom, $D(\omega)$ is the vibrational density of states per unit volume and ω is the phonon frequency [21]. The total energy dependent vibrational density of states is given by a sum over all phonon branches b.

3.1.2 Density of States

Bloch theorem states that observable quantities in the crystal such as charge density and wave function are periodic. Based on Born-von Karman periodic boundary condition, in combination with the Bloch theorem, the number of available states in the crystal are discrete and countable. Density of states (DOS) is the function responsible for calculating the number of available states for storing energy in the crystal. DOS is defined as the number of states per unit volume. However we are more interested in defining it in terms of energy or frequency. In an isotropic crystal, we need to calculate the phonon DOS using the Debye approximation. In a 3D solid, Debye approximation expresses that in the center of the Brillioun Zone (uniquely defined primitive cell in reciprocal lattice space) the dispersion is proportional to the

speed of sound. In a more general case, the crystal can be anisotropic, hence the DOS can be calculated by the sum over all phonon branches as:

$$D(\omega) = \sum_{\mathrm{b}} \int \frac{d\vec{q}}{(2\pi)^3} \delta\left[\omega - \omega_{\mathrm{b}}(\vec{q})\right]. \tag{3.7}$$

The volume integral of the energy-conserving delta function over the whole first Brillouin zone is calculated from the full phonon dispersion using the method of Gilat and Raubenheimer [22].

3.1.3 Equilibrium Distribution Functions

Total energy of the crystal can be obtained using Density of States. In order to calculate the energy that can be stored in the crystal, we need to apply the distribution function to determine if states of energy are occupied. Distribution functions for electrons follow the Fermi Dirac distribution while phonons follow the Bose Einstein distibution function.

$$f_{FD}(E,T) = \frac{1}{exp(\frac{E-E_F}{K_B T}) + 1} \tag{3.8}$$

$$f_{BE}(E,T) = \frac{1}{exp(\frac{\hbar\omega}{K_B T}) - 1} \tag{3.9}$$

Utilizing the particular distribution function for electrons and phonons, total energy can be calculated.

3.1.4 Isotope Scattering

A similar expression as Eq. 3.5 holds for isotope and impurity scattering within each material in the alloy [32]. The contribution due to isotopic variation in each of the constituent materials can be obtained by combining the isotope constants for each pure material as:

$$\Gamma_{\mathrm{Iso}}(x) = \frac{(1-x-y)\Gamma_{\mathrm{Si}} M_{\mathrm{Si}}^2 + x\Gamma_{\mathrm{Ge}} M_{\mathrm{Ge}}^2 + y\Gamma_{\mathrm{Sn}} M_{\mathrm{Sn}}^2}{\left(xM_{\mathrm{Ge}} + (1-x-y)M_{\mathrm{Si}} + yM_{\mathrm{Sn}}\right)^2}, \tag{3.10}$$

where the pure silicon and germanium isotope scattering constants Γ_{Si} and Γ_{Ge} were taken from Ref. [38]. The tin isotope scattering constant Γ_{Sn} has a value of 3.64, which was calculated based on the known isotope composition of Sn. An additional component to alloy scattering arising from the strain field, due to the difference in lattice constants of pure Si and Ge and their alloys, has been proposed.

3.1.5 Strain Scattering

The contribution due to strain is given by [2]

$$\Gamma_{\mathrm{Strain}} = \epsilon \sum_i f_i (1 - a_i/\bar{a})^2, \tag{3.11}$$

where f_i is the proportion of material i with lattice constant a_i (in this case Si, Ge and Sn), while the average lattice is $\bar{a} = \sum_i f_i a_i$. Composition-dependent alloy lattice constant ($a_{\mathrm{SiGeSn}}(x)$) taken in the virtual crystal approximation, including bowing parameter [44]. The empirical strain parameter is taken to be $\epsilon = 39$ [1]. For most values of germanium concentration x, the strain contribution $\Gamma_{\mathrm{Strain}}(x)$ is found to be much smaller than the mass-difference component.

3.1.6 Umklapp Scattering

The resistive umklapp phonon- rate was calculated in the standard general approximation for dielectric crystals [38]

$$\tau_{\mathrm{b,U}}^{-1}(\vec{q}) = \frac{\hbar \gamma_{\mathrm{b}}^2}{\overline{M} \Theta_{\mathrm{b}} \bar{v}_{\mathrm{b}}^2} \omega_{\mathrm{b}}^2(\vec{q}) T e^{-\Theta_{\mathrm{b}}/3T}, \tag{3.12}$$

where the speed of sound $\bar{v}_{\mathrm{b}}$ of each branch b is determined from the average slope of its dispersion curve near the Γ point, and $\overline{M}$ is the average atomic mass. The Grüneissen parameter γ_{b} was obtained for each branch from the phonon dispersion. It has a value of 1.1 for the longitudinal acoustic branch and -0.6 for the transverse acoustic branches. The expression in Eq.3.12 contains the exponential term $e^{-\Theta_{\mathrm{b}}/3T}$ in

the temperature dependence, which controls the onset of resistive umklapp scattering for each phonon branch through the branch-specific Debye temperatures, Θ_λ, which were obtained from [48]

$$\Theta_{\mathrm{b}}^2 = \frac{5\hbar^2}{3k_B^2} \frac{\int \omega^2 g_{\mathrm{b}}(\omega) d\omega}{\int g_{\mathrm{b}}(\omega) d\omega}, \tag{3.13}$$

where the vibrational density of states (vDOS) function $g_{\mathrm{b}}(\omega) = \sum_{\mathrm{b},\vec{q}} \delta\left[\omega - \omega_{\mathrm{b}}(\vec{q})\right]$ was calculated for each phonon branch b from the full dispersion. Using this method, the temperature dependence of the contribution from each phonon branch to the total thermal conductivity is correctly represented.

CHAPTER 4

THERMAL CONDUCTIVITY OF BULK AND NANOSTRUCTURE ALLOYS

4.1 Thermal Conductivity of Bulk Alloys

In the bulk case, the crystal is assumed to be infinite and uniform. There are no boundaries and interfaces in the material. The distribution is only a function of temperature and in the absence of boundaries and interfaces, the solution of the pBTE equation is simply given by

$$n_{\vec{q}} = \tau_{int.}(\vec{q})\vec{v}_{\vec{q}} \cdot \nabla_{\vec{r}} T \frac{\partial N^0_{\vec{q}}(T)}{\partial T}. \tag{4.1}$$

The lattice thermal conductivity of bulk ternary alloy SiGeSn was calculated from the full dispersion pBTE model discussed previously. The plot in Fig. 4.1 depicts thermal conductivity of bulk SiGeSn alloys against their contributed composition. Thermal conductivity of binary alloys SiGe, SiSn, and GeSn can also be seen along the edges where Ge, Si, and Sn compositions equal to zero for SiSn, GeSn, and SiGe, respectively. Also, at the corners thermal conductivity of pure Si, Ge and Sn is depicted when the composition of the other two constituents are zero. We note here that the broad plateau which thermal conductivity reaches in the alloy composition range of $0.2 < x < 0.8$ for germanium composition in $Si_{1-x}Ge_x$ and $0.2 < y < 0.8$ for tin composition in $Si_{1-y}Sn_y$, and a similar plateau for GeSn, have limited the amount of reduction in lattice thermal conductivity which can be achieved through alloying alone.

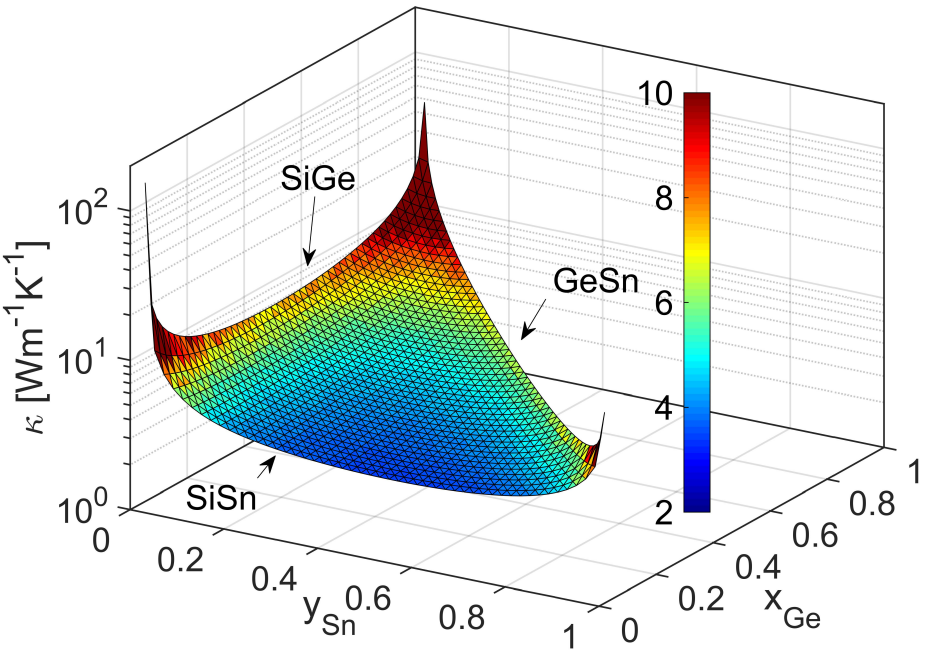

Figure 4.1. 3D plots of thermal conductivity vs. Sn and Ge composition (y_{Sn} and x_{Ge} respectively) for SiSn, GeSn and SiGe of bulk material at room temperature. SiSn has the lowest thermal conductivity in the bulk form [27].

The reason for this broad plateau is related to the dominant mass disorder scattering in alloys which depends on the difference in atomic mass between the constituent materials and the average mass. However, our results, as shown in Fig. 4.1, demonstrate that adding Sn into the alloy causes further reduction of thermal conductivity below the minimum value achievable in SiGe. The lowest thermal conductivity for bulk binary alloys SiSn and GeSn are 3 W/mK, reached at Sn composition of 0.51, and 5.86 W/mK at Sn composition of 0.61, respectively. These values are significantly lower than the lowest thermal conductivity of bulk SiGe, which is 6.7 W/mK at Ge composition of 0.34. Among these alloys, the binary SiSn alloy is found to have the lowest bulk thermal conductivity, in good agreement with RNEMD calculations at the mass ratio of 4.2 between Si and Sn [20]. The reduction is explained by the larger

mass difference between Si and Sn which results in a higher mass disorder scattering rate, hence a lower lattice thermal conductivity [55]. Bulk SiSn alloys at such a high Sn concentration have not been demonstrated experimentally due to the low solid solubility of Sn in Si; nonetheless, thermal conductivity at 18% Sn concentration, the highest Sn fraction demonstrated in a far [29], is 4.71 W/mK, which is nearly a 50% reduction from the lowest bulk SiGe value.

4.2 Minimum Achievable Thermal Conductivity

The behavior of thermal conductivity as the thickness is reduced to the nanoscale can be altered based on the model and assumptions used. Cahills minimum thermal conductivity model [12] implies that the scattering rate has an upper bound (while only approximate and not necessarily a general lower bound) [19]. This bound can be obtained when the phonon lifetime equals one-half period of the vibrational frequency. Hence, the upper bound on the scattering rate is given by $\tau_{max}^{-1} = \omega/\pi$. In a crystal, this theoretical minimum value would be achieved by having maximum disorder while bulk vibrational modes are retained. Utilizing this maximum scattering rate (Cahills minimum thermal conductivity model), experimental values for amorphous Si (1 W/mK), Ge (0.6 W/mK) and Sn(W/mK) have been achieved. We contrast the bulk alloy results to their corresponding theoretical minimum values, often called the amorphous limit. The calculations provide us with some indication of what conductivity might be achievable through disorder (mass/alloy or boundary roughness) in a crystalline material. The calculated amorphous (disordered) thermal conductivity of ternary alloys of SiGeSn are shown in the Fig. 4.2. Unlike the bulk results, there is no plateau and pure Sn has the lowest achievable thermal conductivity in comparison with all other alloy compositions due to its lowest vibrational frequencies of the three materials. We find that the amorphous limit values are all below 1 W/mK; conse-

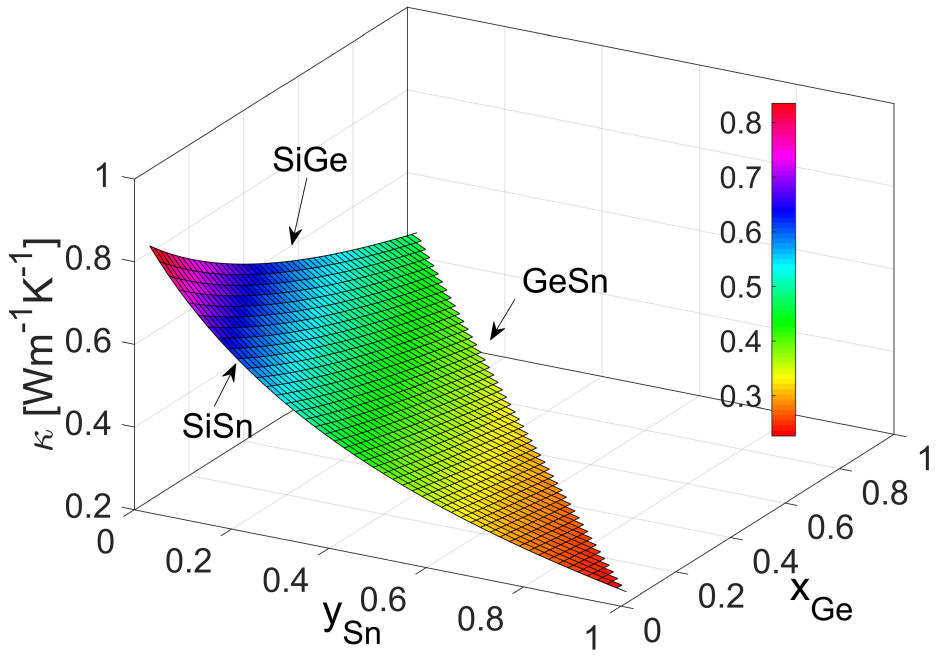

Figure 4.2. 3D surface plot of lowest achievable thermal conductivity vs. alloy compositions for SiGeSn at room temperature. Binary alloys correspond to the edges of the triangle of data points, showing that Sn has the lowest thermal conductivity in the amorphous (disordered) limit [27].

quently, there is room to reduce the thermal conductivity further through size effects caused by boundary roughness scattering in nanostructures.

4.3 Thermal Conductivity in Low-dimensional Alloys

In this part, we study and compared the cumulative thermal conductivity of pure Si, Ge, and Sn with their corresponding binary alloys. These results help us figure out the extent to which size scaling can reduce the thermal conductivity.

4.3.1 Cumulative Thermal Conductivity

In this section, the cumulative thermal conductivity is scaled by the total thermal conductivity so that it shows how lattice thermal conductivity is accumulated against

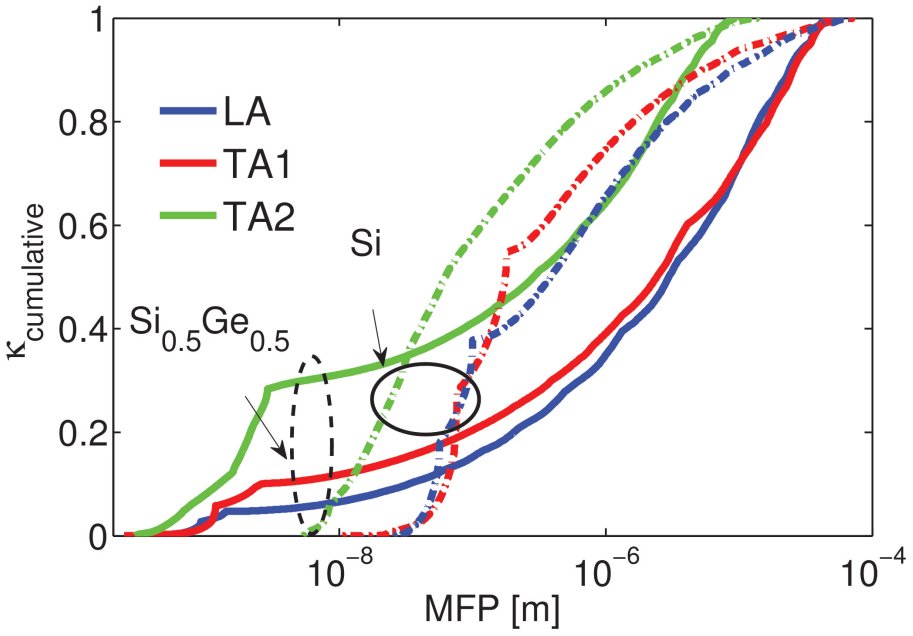

Figure 4.3. Cumulative thermal conductivity of pure Si (dashed lines) and SiGe alloy (solid lines) for acoustic branches [27].

phonon MFP. This allows us to visualize and compare the extent to which restricting the phonon MFP via nanostructuring can result in thermal conductivity reduction [3].

Fig. 4.3 shows the cumulative thermal plot of pure Si and $Si_{0.5}Ge_{0.5}$ bulk alloy vs. mean free path. Fig. 4.4 demonstrates the cumulative thermal plot of pure Si and $Si_{0.5}Sn_{0.5}$ bulk alloy vs. mean free path. Fig. 4.5 depicts the cumulative thermal conductivity vs. mean free path for the pure Ge and $Ge_{0.5}Sn_{0.5}$ bulk alloy. In the mentioned figures solid lines represent a longitudinal and acoustic mode of the bulk alloy while the dashed lines depict the pure material. Comparing pure material with their corresponding alloys in the micro-scale regime shows that alloy materials have lower accumulated thermal conductivity. Therefore, decreasing the size down to the nanoscale regime (below the MFP) can result in the reduction of thermal conductivity.

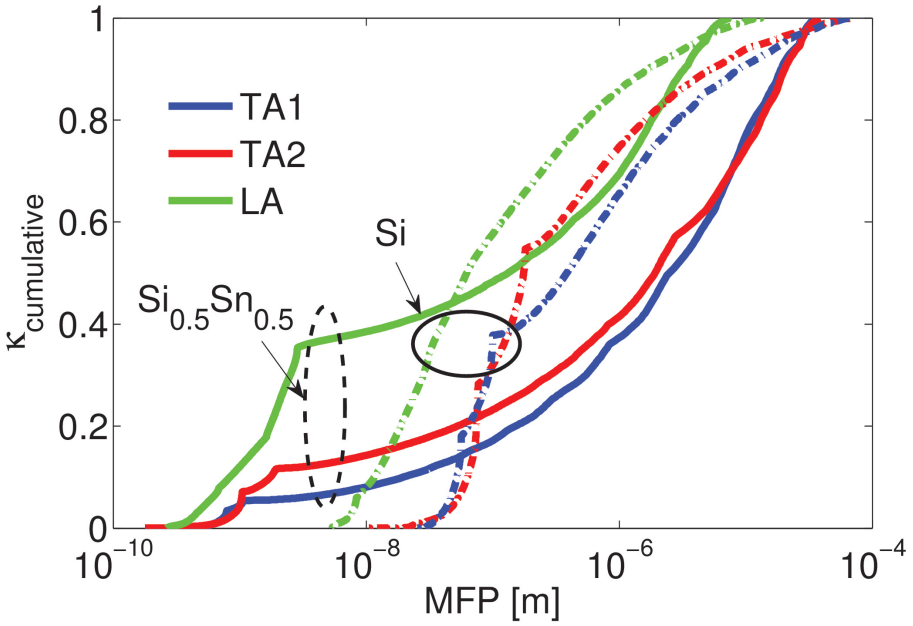

Figure 4.4. Cumulative thermal conductivity vs. mean free path of pure Si (dashed lines) and SiSn alloy (solid lines) [27].

Because the density of states peaks near van Hove singularities which is a non-smooth point in the DOS of the first Brillouin zone (BZ), there are sharp bends in the slope of the cumulative thermal conductivity plot corresponding to these peaks. Throughout these plots, we have focused on the longitudinal and transverse acoustic modes and omitted the optical ones due to their low contribution to thermal conductivity, caused by their very flat dispersion and consequently low phonon group velocities. As a result, we proposed our second approach which is to use low-dimensional nanostructures. This could result in reduction of thermal conductivity and become further closer to the amorphous limit.

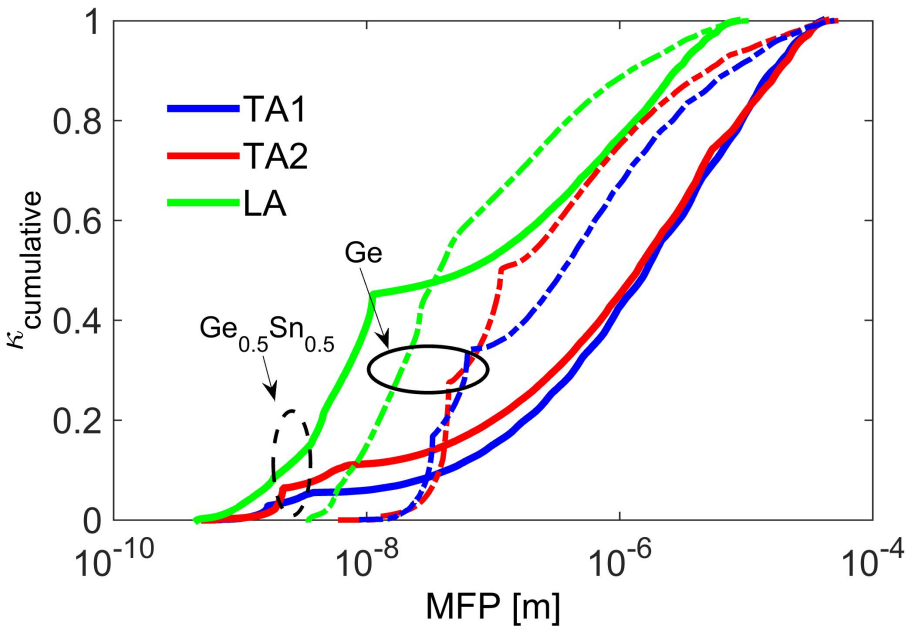

Figure 4.5. Cumulative thermal conductivity vs. mean free path of pure Ge (dashed lines) and GeSn alloy (solid lines) [27].

4.3.2 Boundary Scattering

In the bulk due to the two assumptions of being infinite and uniform, boundaries and interfaces have been neglected. However, boundaries and interfaces play an important role in the solution of pBTE in nanostructures. Hence, in nanostructures, we have to add an extrinsic relaxation rate $\tau_{\mathrm{b,B}}^{-1}(\vec{q})$ due to boundary roughness (B) scattering. We study this phenomena by attributing probability to the phonons that are being scattered by "1-p" or not being scattered by "p". Each time a phonon reaches the boundary, we capture the probability of it not being scattered by the roughness through the momentum-dependent specularity parameter $0 < p(\vec{q}) < 1$ given by:

$$p(\vec{q}) = \exp\left(-4\Delta^2 q^2 \cos^2\Theta\right) \tag{4.2}$$

with Δ being the rms boundary roughness (typically $0.1 < \Delta < 1$ nm, depending on sample quality and processing) and Θ being the angle between the direction of

propagation of the phonon wave and the boundary normal. The specularity parameter allows us to capture both the magnitude and the angle dependence of the scattering and distinguish between the contribution to the heat flux from phonons traveling into the boundary (small Θ, hence smaller $p(\vec{q})$ and more scattering) and phonons traveling parallel to the boundary (large Θ and larger $p(\vec{q})$, leading to less scattering). The specularity parameter is used in solving the pBTE as a boundary condition, with $[1 - p(\vec{q})]$ giving the fraction of the incoming phonons which are scattered randomly. As boundary scattering is a momentum-randomizing elastic process, the scattered phonons will carry zero heat flux, so they can be represented by the equilibrium Bose-Einstein distribution (which was discussed in detail in Section 3.1.3), leading to a boundary condition of the form:

$$N_{\mathrm{b}}(\vec{q})^{+} = p(\vec{q}) N_{\mathrm{b}}(\vec{q})^{-} + [1 - p(\vec{q})]\, N^{0}_{\mathrm{b},T}(\vec{q}). \tag{4.3}$$

with + and - representing the solution before reaching and after leaving the boundary respectively, and $N_0(\vec{q})$ is the equilibrium Bose-Einstein phonon distribution of phonon mode $\vec{q}$ in branch b. The boundary scattering rate for a film of thickness H is then obtained as [6]:

$$\tau^{-1}_{\mathrm{b,B}}(\vec{q}) = \frac{\upsilon_{\mathrm{b},\perp}(\vec{q})}{H} \frac{F_p(\vec{q}, H)}{1 - \frac{\tau^{int}_{\mathrm{b}}(\vec{q})\upsilon_{\mathrm{b},\perp}(\vec{q})}{H} F_p(\vec{q}, H)}, \tag{4.4}$$

where a mode-dependent scaling factor $F_p(\vec{q}, H)$ is given by:

$$F_p(\vec{q}, H) = \frac{[1 - p(\vec{q})]\,\{1 - \exp\left[-H/\tau^{int}_{\mathrm{b}}(\vec{q})\upsilon_{\mathrm{b},\perp}(\vec{q})\right]\}}{1 - p(\vec{q}) \exp\left[-H/\tau^{int}_{\mathrm{b}}(\vec{q})\upsilon_{\mathrm{b},\perp}(\vec{q})\right]}. \tag{4.5}$$

This formulation of interface scattering allows for the rates of internal (intrinsic) and boundary roughness scattering to be added together, despite of their interdependence [56]. The factor given by Eq. 4.5 encapsulates the competition between the boundary and internal scattering: the effective strength of boundary scattering

will depend on the relative strength of the competing internal scattering mechanisms [52]. The full thermal conductivity tensor $\kappa^{\alpha\beta}$ is obtained as a sum over all phonon momenta and branches [28]

$$\kappa^{\alpha\beta} = \sum_{\mathrm{b},\vec{q}} \tau_{\mathrm{b}}(\vec{q}) C_{\mathrm{b},T}(\vec{q}) \upsilon_{\mathrm{b}}^{\alpha}(\vec{q}) \upsilon_{\mathrm{b}}^{\beta}(\vec{q}), \tag{4.6}$$

where $\tau_{\mathrm{b}}(\vec{q})$ is the total phonon relaxation time [for a bulk sample, $\tau_{\mathrm{b}}(\vec{q}) = \tau_{\mathrm{b,Internal}}(\vec{q})$ from Eq. 3.3] and the phonon heat capacity per mode $C_{\mathrm{b},T}(\vec{q})$ is given by:

$$C_{\mathrm{b},T}(\vec{q}) = \frac{[\hbar\omega_{\mathrm{b}}(\vec{q})]^2}{k_B T^2} \frac{e^{(\hbar\omega_{\mathrm{b}}(\vec{q})/k_B T)}}{[e^{(\hbar\omega_{\mathrm{b}}(\vec{q})/k_B T)} - 1]^2}. \tag{4.7}$$

$\upsilon_{\mathrm{b}}^{\alpha}(\vec{q})$ is a component of the phonon velocity vector calculated from the full phonon dispersion based on Weber's adiabatic bond charge (ABC) model [61] which was discussed in chapter 3.

4.4 Results and Discussions on Phonon Transport in Nanostructures

In this section pBTE in the RTA for nanostructures including the extrinsic boundary scattering has been solved to observe the thermal conductivity reduction from bulk to nanostructure. This study includes calculation of the lattice thermal conductivity of thin alloy films for binary SiGe, GeSn and SiSn and ternary SiGeSn to further decrease the thermal conductivity towards the amorphous limit.

4.4.1 Binary Alloys

The results of our calculations for thin SiGe alloy films are depicted in the plot of Fig. 4.6; these results have been validated through comparison with experimental data from Cheaito et al. [14, 39]. Overall the trends follow the expected reduction due to extrinsic boundary scattering in thin films. We include SiGe results here mainly for comparison with our new results in Fig. 4.7 and Fig. 4.8 for SiSn and GeSn

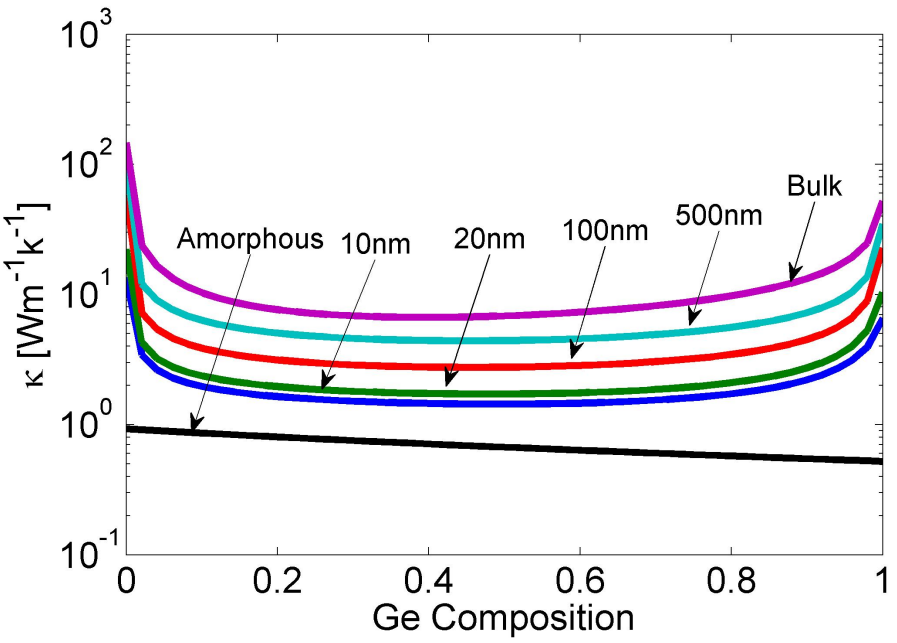

Figure 4.6. Lattice thermal conductivity of binary alloy SiGe vs. Ge composition for bulk, 500 nm, 100 nm, 20 nm and 10 nm thickness at room temperature. The sample thickness is 1 μm for nanostructures with 0.45 nm roughness. The bottom line shows the lowest achievable thermal conductivity- amorphous limit- of SiGe vs. Ge composition [27].

respectively. Comparing the results across compositions at a fixed film thickness, we find that the thermal conductivity SiGe thin alloy films reach the lowest value of 1.718 W/mK at 20 nm thickness for Ge composition of 0.46 and 1.43 W/mK at 10 nm thickness for Ge composition of 0.51. In contrast, the lowest thermal conductivity for SiSn at 20 nm thickness is 0.91 W/mK, achieved at Sn composition of 0.59 Sn. Such high Sn compositions exceeding 18% may be achievable in very thin films; however, we note here that at 0.18 Sn composition and 10 nm thickness, the thermal conductivity only increases to 1.10 W/mK because of the broad plateau in thermal conductivity vs. composition which can be seen in Fig. 4.7. This value still represents nearly a 30% reduction from the lowest value achievable in SiGe thin films of equal 20 nm thickness.

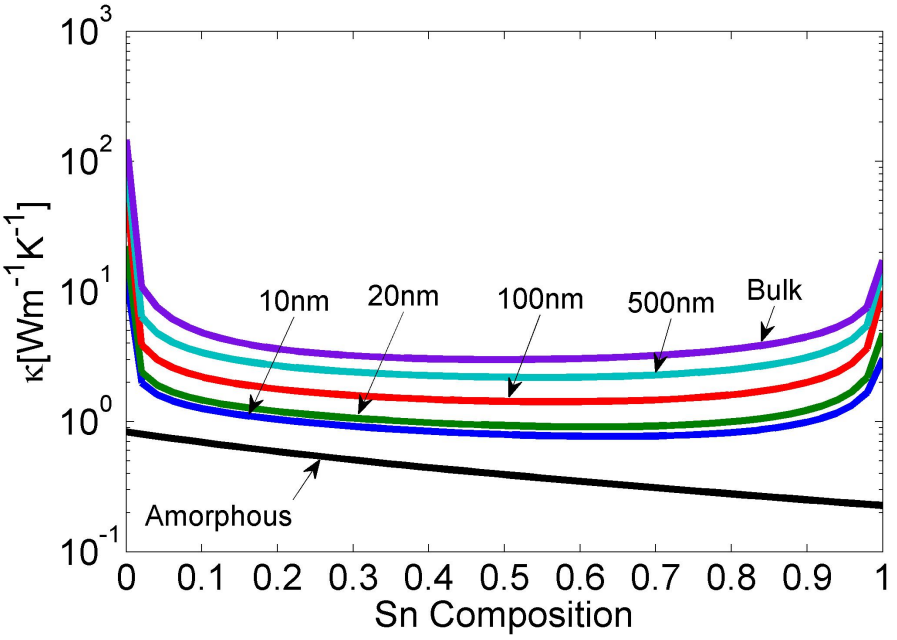

Figure 4.7. Lattice thermal conductivity of binary alloy SiSn vs. Sn composition for bulk, 500 nm, 100 nm, 20 nm and 10 nm thickness. The simulation is done at room temperature with the roughness of 0.45 nm and sample thickness of 1 μm for nanostructures. The bottom line depicts the amorphous limit thermal conductivity of the alloy against Sn composition while the top line shows thermal conductivity of bulk SiSn [27].

For GeSn thin films, shown in Fig. 4.8, the lowest thermal conductivity value in 20 nm films is 1.53 W/mK at Sn composition of 0.57. Reducing the thickness further down to 10 nm, our model shows that the thermal conductivity becomes even closer to the amorphous limit. For GeSn, the lowest value achieved in a 10 nm thin film is 1.24 W/mK, obtained at Sn composition of $y = 0.59$. The thermal conductivity of SiSn alloy films is lower than the other two binary alloys owing to the larger difference in mass between Si and Sn, as compared to that of Ge and Sn. Epitaxial GeSn and ternary SiGeSn alloy layers on Si have been demonstrated and employed in the literature [9, 16] with larger Sn concentration than their SiSn counterparts. As it was expected, boundary scattering and mass scattering (which is higher in the SiSn) results in further decrease in thermal conductivity toward the amorphous limit.

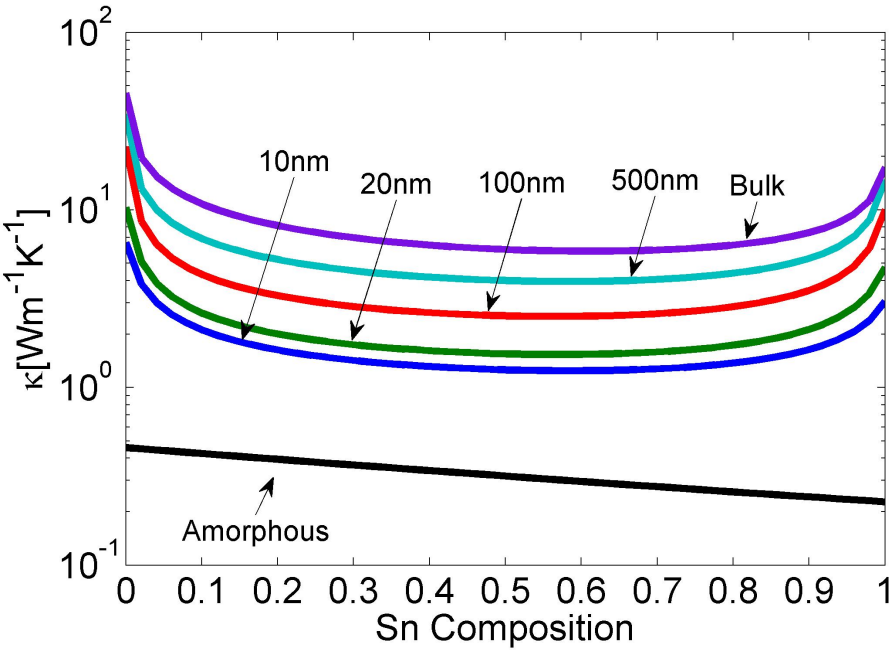

Figure 4.8. Lattice thermal conductivity of binary GeSn vs. Sn composition for bulk, 500 nm, 100 nm, 20 nm and 10 nm thickness. The simulation is done at room temperature with roughness of 0.45 nm and 1 μm in-plane sample length. The bottom line depicts the amorphous limit thermal conductivity of the alloy against Sn composition while the top line shows thermal conductivity of bulk SiSn [27].

4.4.2 Ternary Alloy

Cumulative contributions to thermal conductivity vs. phonon mean free path has also been depicted in the Fig. 4.9 which shows that alloying leads to a broader range and a more gradual dependence on mean free paths, allowing us to further decrease the thermal conductivity through nanostructuring. In Fig. 4.10, we depict the thermal conductivity of ternary alloy vs. Ge and Sn composition. We have assumed that germanium and tin compositions, x and y respectively, are equal ($x = y$) and are varying from 0 to 0.5 while the silicon composition $(1 - x - y)$ is reduced from 1 to 0. At germanium and tin compositions of $x = y = 0.32$ and the film thickness of 10 nm, the thermal conductivity reaches its lowest value of 0.93 W/mK, which is lower than the SiGe thermal conductivity at the same thickness, but slightly higher than

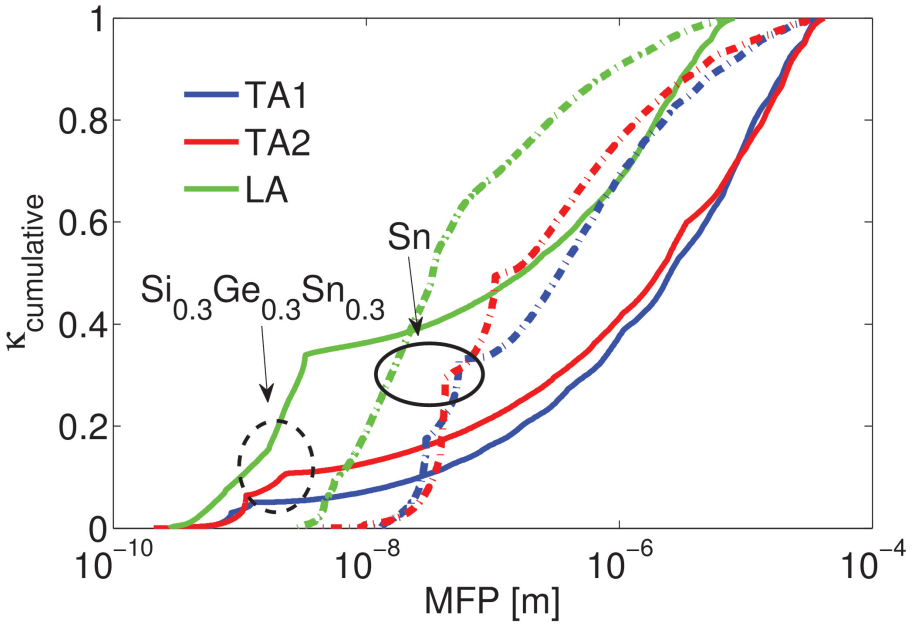

Figure 4.9. Cumulative thermal conductivity vs. mean free path of pure Sn (dashed lines) and $Si_{0.3}Ge_{0.3}Sn_{0.3}$ alloy (solid lines) [27].

the lowest value achieved in SiSn at that same thickness. However, this is the closest value to the lowest achievable thermal conductivity given by the amorphous limit.

4.5 Summary of the Thermal Conductivity in Bulk and Nanostructure

The goal of this thesis is to improve the overall conversion efficiency of thermoelectric devices (which have the ability to harvest electricity from waste heat). To improve the efficiency, ZT needs to become greater in size. Therefore, initially, the main study was to focus on decreasing the thermal conductivity in the denominator of ZT. In this work, we have concentrated on group IV semiconductor materials including binary SiGe, SiSn, and GeSn, as well as ternary SiGeSn bulk and nanostructure alloys. The lattice contribution to thermal conductivity, in binary and ternary group-IV alloys, has been calculated by solving phonon Boltzmann transport equation in the relaxation

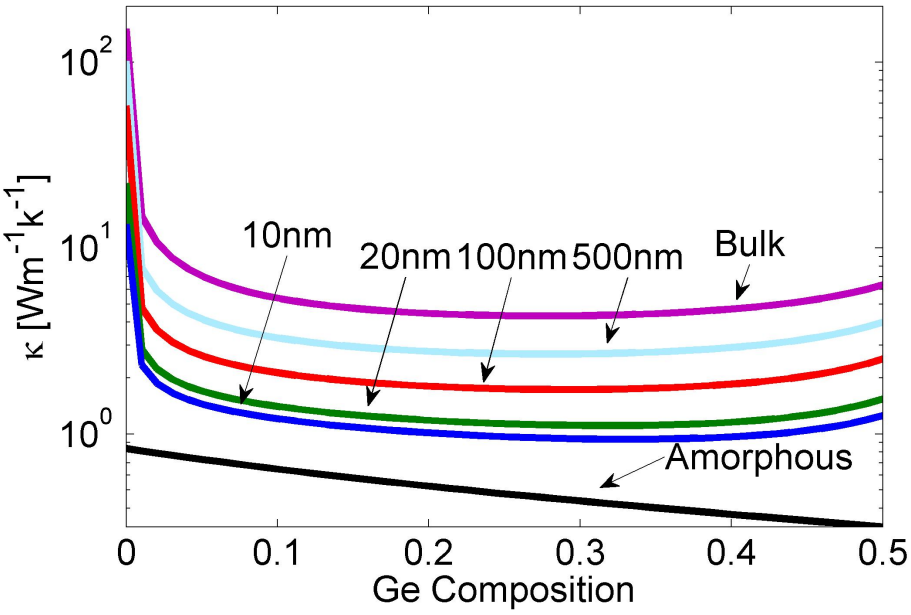

Figure 4.10. Lattice thermal conductivity of ternary of alloy SiGeSn vs. Ge or Sn composition for bulk, 500 nm, 100 nm, 20 nm and 10 nm thickness at room temperature with 0.45 nm roughness and 1 μm in-plane film length. The bottom black line shows the lowest achievable thermal conductivity of the alloy against Ge or Sn composition [27].

time approximation. In this calculation, all intrinsic scattering mechanisms (3-phonon umklapp and normal, isotope, impurity, and mass-difference alloys scattering) as well as interactions with partially diffused boundaries of the nanostructures described by a momentum dependent model for phonon scattering with boundary roughness have been considered. In addition, the full phonon dispersion computed from the adiabatic bond charge model was combined by the phonon dispersions for alloys in the virtual crystal approximation. Significant reduction in the thermal conductivity cumulative plot of alloy material in comparison with pure material demonstrates that thermal conductivity is tunable by both thickness and alloying over a wide range of values. Among the materials under study Si and Sn have the largest mass difference, leading to the highest mass scattering in the SiSn alloy of all the binary combinations, and

hence the lowest thermal conductivity. In nanostructures, there is a further reduction in thermal conductivity due to size effects to values far below the bulk and almost to the amorphous limit. Our results demonstrate that binary and ternary group IV alloys involving Sn have low lattice thermal conductivity, and therefore may have potential as high-efficiency TE materials, especially in nanostructured form.

CHAPTER 5

ELECTRON TRANSPORT

Having the thermal path data reduced by alloying and nanostructuring approaches, the next step of this thesis is to study electrical path including Seebeck coefficient (S), electrical conductivity (σ), and electronic contribution of thermal conductivity (κ_{el}) of these materials. In the first part of this study, we used the full phonon dispersion to calculate the thermal conductivity (κ_{ph}). Thus, in this part of the study, we have calculated full electron band structure for different compositions of SiGe alloys to allow integration with the first part. Si and Ge have the bottom of conduction band near the Δ and L point respectively; two completely different directions. The bandstructure changes tremendously from Si to Ge with alloying and the bandgap reduces from 1.1 to 0.6 eV. Subsequently, the location and energy of the conduction band minimum will change with the composition. Hence, it is required to calculate the bandstructure for each composition. In this study, we have calculated 13 bandstructures ranging between Ge composition of 0 and 1. A dense grid of wave vector ($\vec{k}$) within the first BZ has taken to calculate the corresponding energies. The electron velocities for each of the wave vector ($\vec{k}$) are obtained by finite differences method. In our model, both the Δ and L conduction minima and their relative positions with respect to the germanium composition have been considered. When calculating electrical properties, BTE needs to be solved by including all elastic and inelastic scattering mechanisms. The iterative Rodes method can be used to calculate the perturbed distribution function. Having the data on thermal conductivity along with the power factor, we can find a range of compositions and thicknesses in

which the highest ZT can be achieved in the materials under study. These results can be utilized to design next generation of thermoelectric converters that will enable us to recover significant amounts of waste heat back into useful electric energy with higher efficiency. The question is whether the thermoelectric properties of SiGe can be further improved by changes in composition, doping, thickness, and temperature.

5.1 Rode's Method for Electron Mobility Calculation

As symmetry plays an important role, usually the distribution functions is split into symmetric and anti-symmetric part. In the case of anisotropic and inelastic scattering, the RTA can not be applied for solving BTE. Instead, Rode's iterative method can be used for calculating the actual distribution function under the low field. Rode's method is an iterative method widely used in calculating mobility of carriers. Applying a low field or temperature gradient results in a linear difference equation for the perturbed part of the distribution function [45]. In this method, perturbation in distribution function is iteratively solved to calculate the mobility of the carriers. This approach is used in the case that the scattering process is inelastic and anisotropic in which RTA can not be used. In the inelastic and anisotropic case, it is almost impossible to define a simple relaxation time that does not depend on the distribution function because the distribution of carriers does not relax to their equilibrium distribution. In the Rode's method inelastic scattering of carriers are effectively implemented to capture the perturbation to the distribution function under low-field condition.

In our model, BTE is solved by including alloy scattering and the effect of separate Δ and L bands similar to the approach used in the Ref. [10]. In order to do so, the distribution function is approximated to the first order using Lagrange polynomials and only linear terms have been kept (shown in equation 5.1).

$$f(x) = f_0(k) + g(k)cos\theta \tag{5.1}$$

where $f_0(k)$ is the equilibrium distribution function, $g(k)$ is the perturbation to the distribution function and θ is the angle between velocity and the applied electric field. Having the approximated distribution function, the BTE including the inelastic scattering rate is iteratively solved to calculate the perturbed distribution function shown in the equation 5.2. This calculation continues until the result converges. In our model, successive iteration differs by a tolerance defined as 10^{-3} from the previous iteration. Usually few iterations are required to satisfy this condition as the convergence proceeds exponentially. This formalism is valid only for low electric fields [45]. The perturbation to the distribution function is defined below, which is taken form Ref. [57] to include the in-scattering rate of inelastic rate and the total scattering rate:

$$g_{i+1} = \frac{S_{i0}g_i - \frac{eF}{\hbar}\frac{\partial f_0}{\partial k}}{S_0} \tag{5.2}$$

g_i will be referred to as the perturbation distribution. g_{i+1} which is the $(i+1)^{th}$ solution is calculated using i^{th} iteration solution (g_i) of the perturbed distribution function. In this equation, S_{i0} is the in-scattering rate of inelastic scattering and S_0 is the total out-scattering rate.

The Rode's method immediately gives RTA solution for elastic and isotropic cases (zeroth solution) in which in-scattering rates vanishes. Implementing the Eq. 5.2 into the isotropic mobility expression discussed in the Ref. [15], the mobility for anisotropic case can be obtained be equation below:

$$\mu_e = \frac{\int\int v(k)g_i(k)\delta(E - E(k))dk}{F\int\int f(k)\delta(E - E(k))dk} \tag{5.3}$$

where $v(k)$ is the group velocity and F (eE) is the electric force. Having the electron mobility, the electrical conductivity (σ) and electrical contribution to thermal conductivity κ_{el} can be achieved. Having the electron mobility, σ and κ_{el} can be achieved.

Seebeck coefficient derives from continuity equations, passing carrier densities into the current operators [62]. The Seebeck coefficient is obtained by implementing Eq. 5.2 into the isotropic expression for Seebeck coefficient in the Ref. [15]. Hence, the Seebeck coefficient is calculated using the expression below:

$$S = \frac{\int\int v(k) g_i(k) \delta(E - E(k)) dk}{T \int\int v(k) g_i(k) \delta(E - E(k)) dk} \tag{5.4}$$

5.1.1 Wiedemann-Franz Law

The Wiedemann-Franz law (FWL) is typically used to estimate to what extent the electron has contributed to the thermal conductivity [15]. This law, shows the interdependence of κ_{el}, σ, and T to a Lorenz number (L) which is shown below:

$$L = \frac{\kappa_{el}}{\sigma T} \tag{5.5}$$

Lorenz number is typically close to the value of 2.45×10^{-8} ($W\Omega K^{-2}$) In the metals that electrons are the primary heat carriers, it can be used to directly calculate the thermal conductivity from electrical conductivity, but in the semiconductors it slightly changes depending on the doping level [15].

5.2 Scattering Rates

The elastic and inelastic scattering rates that are included in the Rode's code are introduced in this section. The elastic scatterings are ionized impurity scattering, deformation potential acoustic phonon scattering, boundary scattering, and alloy scattering (in the case of alloy such as SiGe). The inelastic scattering rates are intervalley optical phonon scattering including f-type and g-type that describes the emitted or absorbed energy when electrons interact with phonons.

5.2.1 Deformation Potential Acoustic Phonon Scattering

The vibration of the crystalline lattice gives rise to phonon scattering. Acoustic phonon scattering rate (Γ^{3d}_{acs}) in Bulk or 3D material is given as [43]:

$$\Gamma^{3d}_{acs} = \frac{2\pi E^2_{adef} k_B T}{\hbar v^2 \rho} DOS(E) \tag{5.6}$$

where E_{adef} is acoustic phonon deformation potential, ρ is density, v is velocity, $DOS(E)$ is density of states.

5.2.2 Impurity Scattering

Impurity scattering arises when the material is doped. This type of scattering is usually dominant at low temperatures. The impurity scattering rate that has been implemented in the code is [43]:

$$\Gamma_{imp} = \frac{Z^2 e^4 N_I}{16\sqrt{2}\pi\epsilon^2 m^{*1/2} E_k^{3/2}} \log\left(1 + \frac{Ze^2 N_I^{1/3}}{4\pi\epsilon E_k}\right) \tag{5.7}$$

where N_I is the number scattering centers created due to the impurities, m^* is effective mass of the material, E_k is the energy of carriers and Z is the number of equivalent valleys. Si has 6 and 8 equivalent respectively. Relative permittivity, ϵ, of Si and Ge are 11.8 and 16.1 respectively.

5.2.3 Boundary Scattering

The boundary scattering rate arises in the case of confinement of material with width L and velocity of carriers perpendicular to the boundary v_z is given as [4]:

$$\Gamma_{boundary} = \left(\frac{1-p}{1+p}\right)\frac{L}{v_z} \tag{5.8}$$

where the specularity parameter p is calculated by

$$p = exp(-4k^2\Delta^2 cos(\phi_B)) \tag{5.9}$$

and k is the wave vector of the electron, Δ is the surface roughness and ϕ_B is the angle between the incident electron with the normal of the boundary. The boundary scattering plays an important role in a case that the thickness of the material is comparable to the MFP. However, in this thesis, the widths of the thin films are not lower than 10 nm which is ten times higher than the MFP of an electron. Hence, this scattering is not a dominant scattering mechanism in the electrical part of our study, though it plays a major role in the thermal part as discussed in the Section 4.3.2.

5.2.4 Intervalley Optical Phonon Scattering

In this study, the scattering of carriers due to their coupling to the phonons which results in emission and absorption has been considered. In calculation of intervalley optical phonon scattering, contributions from other branches as well as the same branch should be considered. f-type and g-type transitions is the transition between parallel and perpendicular valleys respectively [40].

Intervalley optical phonon f-type out-scattering rate (Γ^{3d}_{iop}) in bulk or in a 3D material is given as [43]:

$$\Gamma^{f}_{iop} = \frac{q(Z-2)D^2_{kf}(N^f_{po} + f^{\pm}_f)}{\rho\omega_f} DOS(E \pm E_f) \tag{5.10}$$

where E_f is f-type optical phonon energy, f_f is Fermi-Dirac statistics for electron, N^f_{po} is the Bose-Einstein statistics for f-type optical phonons given by the Eq. 3.9. D_{kf} is f-type optical phonon coupling constant, ω_f is frequency of f-type optical phonons and Z is the number of symmetry directions which is 6 for the Si and 8 for the Ge. '+' denotes absorption of phonon and '-' denotes emission of phonon, the corresponding

change in energy of electron are taken care through Fermi-Dirac statistics. D_{kf} which is a fitted parameter in our model; is assumed to be 2×10^{10} eV/m for Si and 0 eV/m for Ge.

Intervalley optical phonon g-type out-scattering rate (Γ^{3d}_{iop}) in bulk or in a 3D material is given as:

$$\Gamma^{g}_{iop} = \frac{qD^2_{kg}(N^g_{po} + f^{\pm}_g)}{\rho\omega_g} DOS(E \pm E_g) \tag{5.11}$$

where E_g is g-type optical phonon energy, f_g is Fermi-dirac statistics for electron, N^g_{po} is the Bose-Einstein statistics for g-type phonon, ω_g is frequency of g-type optical phonons and D_{kg} is g-type optical phonon coupling constant which is a fitted parameter in our model and is 4×10^{10} eV/m for Si and 6×10^{10} eV/m for Ge.

5.2.5 Alloy Scattering

Alloy scattering (a short-range type interaction) was implemented in the code to capture scattering while the carriers travel in the alloy. Alloy scattering is one of the major scattering mechanisms limiting mobility in alloys, especially at low temperatures. The plateau mobility reaches in the compositions ranging between 0.2 and 0.8 which is shown in the Fig. 6.1 in Section 6.1 demonstrates that the alloy scattering is dominant [36]. This will be explained in more detail in Section 4.4. The alloy scattering for non-parabolic band structure is shown in equation below [57]:

$$\Gamma^{alloy}_{k} = \left[\frac{x(x-1)a_{SiGe}3}{\pi}\right]\left(\frac{D^2_{alloy}}{\hbar^4}\right) d.m^*\sqrt{\gamma_k}(1+2\alpha E_k) \tag{5.12}$$

where x is the alloy composition, a_{SiGe} is the lattice constant of the alloy, D_{alloy} is the scattering potential and d is the lattice disorder. γ_k is defined as [51, 57]:

$$\gamma_k = E_k(1+\alpha E_k) = \frac{\hbar^2k^2}{2m^*} \tag{5.13}$$

To calculate the scattering rate, perturbing Hamiltonian is needed. In the case of constant or harmonic perturbation, the scattering rate is proportional to the DOS. Based on the Fermi's Golden Rule which is derived from perturbation theory, transition probability per unit of time from initial to final states is constant and shown in the equation 5.14 below [40]:

$$\Gamma_{if} = \frac{2\pi}{\hbar} | < f \left| H' \right| i > |^2 DOS \tag{5.14}$$

where $< f \left| H' \right| i >$ is the matrix element of the perturbation H′ between the two states of transition. Hence, equation 5.12 can be written as below:

$$\Gamma_k^{alloy} = \pi x(x-1) a_{SiGe}^3 d \left(\frac{D_{alloy}^2}{\hbar} \right) DOS(E) \tag{5.15}$$

where D_{alloy} is a fitted parameter and equals to 0.35 eV in our model, and d is lattice disorder which is considered 0 for the perfect lattice and 1 for maximum disorder.

CHAPTER 6

THERMOELECTRIC PROPERTIES CALCULATION

6.1 Results and Discussions on Electronic Properties

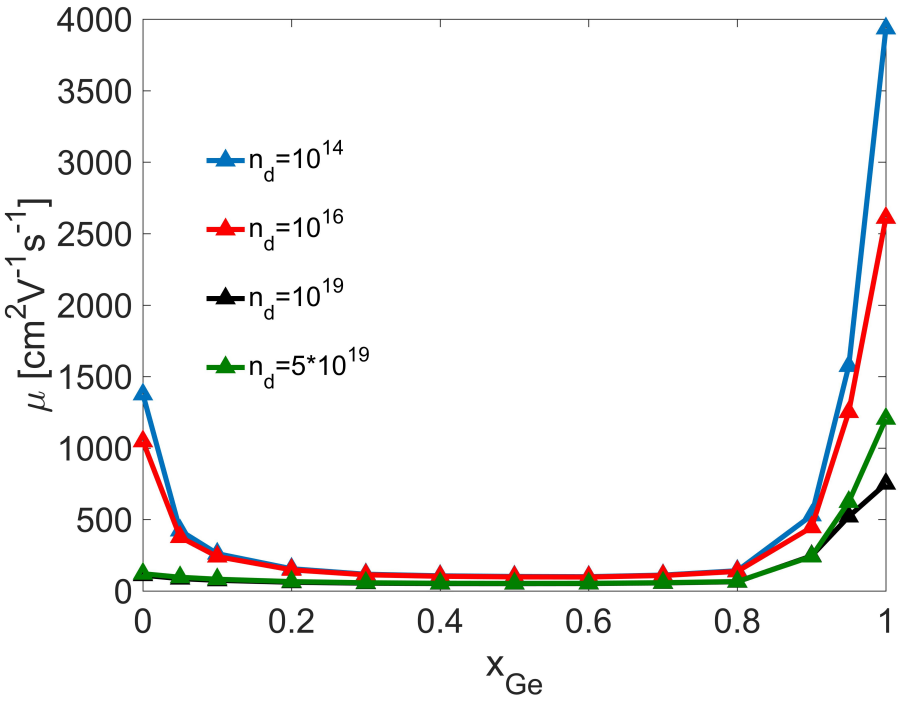

Figure 6.1. Electron mobility vs. Ge composition for n-doped $Si_{1-x}Ge_x$ with donor concentration of 10^{14}, 10^{16}, 10^{19} and 5×10^{19} cm^{-3}. The result at n_d=10^{14} is in good agreement with Ref. [36]

In this part of the study, theoretical calculation of electrical conductivity, Seebeck coefficient, and electrical and lattice contributions to the thermal conductivity is implemented to calculate the ZT. This calculation is specified by band structure, scattering mechanisms and the density of states in a similar fashion as Ref. [51].

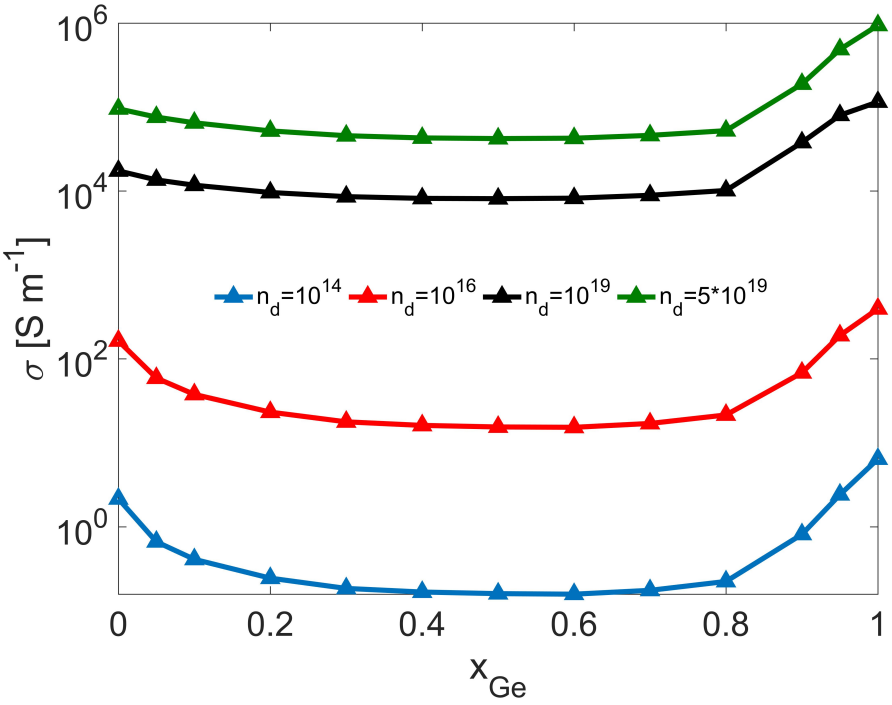

Figure 6.2. Electrical conductivity vs. Ge composition for four carrier concentrations of 10^{14}, 10^{16}, 10^{19} and 5×10^{19} cm^{-3}.

Our results for the electrical path are in good agreement with the bulk experimental results for a broad range of doping concentrations, from 300 K to 1200 K [10] [40].

The results including electronic mobility (μ), electrical conductivity (σ), Seebeck coefficient (S), power factor ($S^2\sigma$), and thermal conductivity (κ_{el} and κ_{ph}) are systematically computed as a function of temperature for different carrier concentrations. Depending on the alloy compositions (whether it is close to the Si or Ge side), The conduction band minimum in $Si_{1-x}Ge_x$ is either at the L or Δ-valley [40]. When the Ge composition equals to the 0.85, the transition between conduction band minima occurs ($Si_{0.15}Ge_{0.85}$). Hence, in our model, we assume this composition as the crossover between Si and Ge.

Fig. 6.1 demonstrates the electron mobility vs. the Ge composition for four different carrier concentrations of 10^{14},10^{16}, 10^{19} and 5×10^{19} cm^{-3}. In our model, we

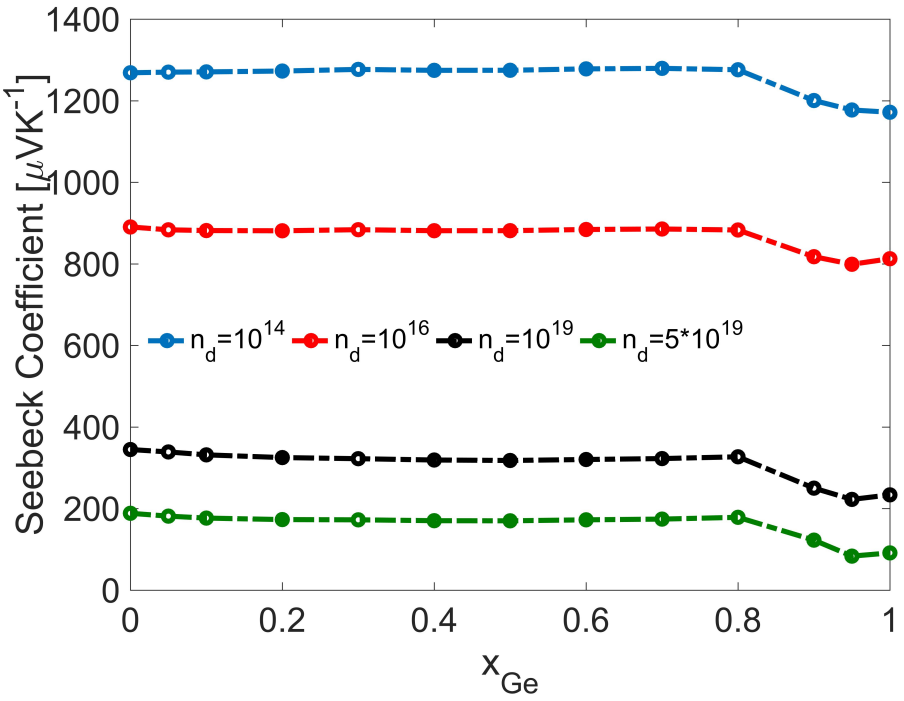

Figure 6.3. Seebeck coefficient vs. Ge composition for four carrier concentrations of 10^{14}, 10^{16}, 10^{19} and 5×10^{19} cm^{-3}.

studied the effect of low and high carrier concentrations to observe the effect of alloying on both extremes. And as a result, we would be able to find the range of optimal concentrations. The alloy electron mobilities calculated in our model have been validated by the theoretical and experimental results for 10^{16} cm^{-3} in Ref. [36] and 10^{14} cm^{-3} in [10] and [40]. The dramatic decrease in the mobility from pure Si to the SiGe alloy and the plateau μ reaches after Ge composition of 0.1 (which continues toward the composition of 0.9) demonstrates that elastic alloy disorder scattering is the dominant scattering mechanisms, except for almost pure Si and Ge. However, in the pure Si and Ge, the acoustic phonon scattering is the most dominant one [40]. In the crossover between L and Δ-valley both elastic and inelastic scattering become important since they are close in energy [40]. As the mobility of the pure Ge is higher

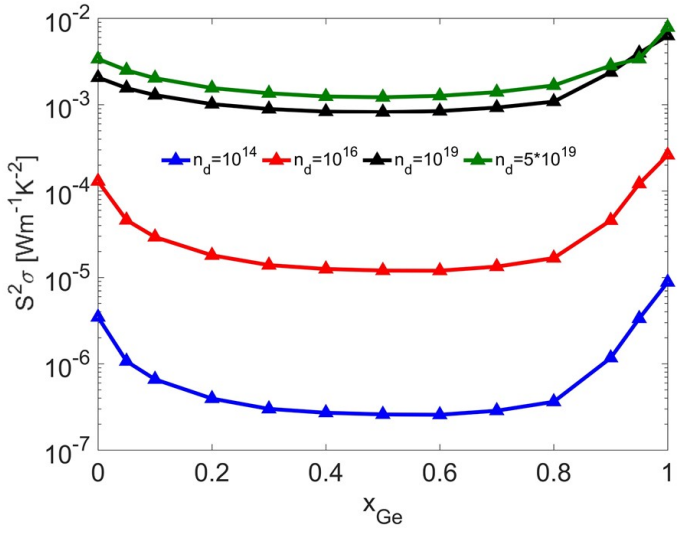

Figure 6.4. Power factor vs. Ge composition for four carrier concentrations of 10^{14}, 10^{16}, 10^{19} and 5×10^{19} cm^{-3}.

than pure Si, the alloys with higher Ge composition ($x_{Ge} > 0.8$) have higher mobility compared to the alloys with higher Si composition.

Fig. 6.2 depicts the electrical conductivity vs. Ge composition for four carrier concentrations of 10^{14}, 10^{16}, 10^{19} and 5×10^{19} cm^{-3}. Alloys with higher doping concentration have higher electrical conductivity. The plateau σ reaches shows the dominance of alloy scattering mechanism. Fig. 6.3 shows the Seebeck coefficient against Ge composition for four carrier concentrations of 10^{14},10^{16}, 10^{19} and 5×10^{19} cm^{-3}. Unlike the electrical conductivity, the Seebeck coefficient decreases by increasing the donor concentrations. The sudden drop at the higher Ge composition (x_{Ge} >0.8) is due to the transition from the Δ to L-valley. The results are in good agreement with the Ref. [8] which only includes the Seebeck coefficient against Si composition for the range of 0 to 0.2 for both low and high carrier concentrations. As electron conductivity values are significantly greater than the Seebeck coefficients, the power factor is mostly governed by σ. This results in increasing power factor with the increase of carrier concentration as shown in Fig. 6.4. Fig. 6.5 shows the electronic contribution

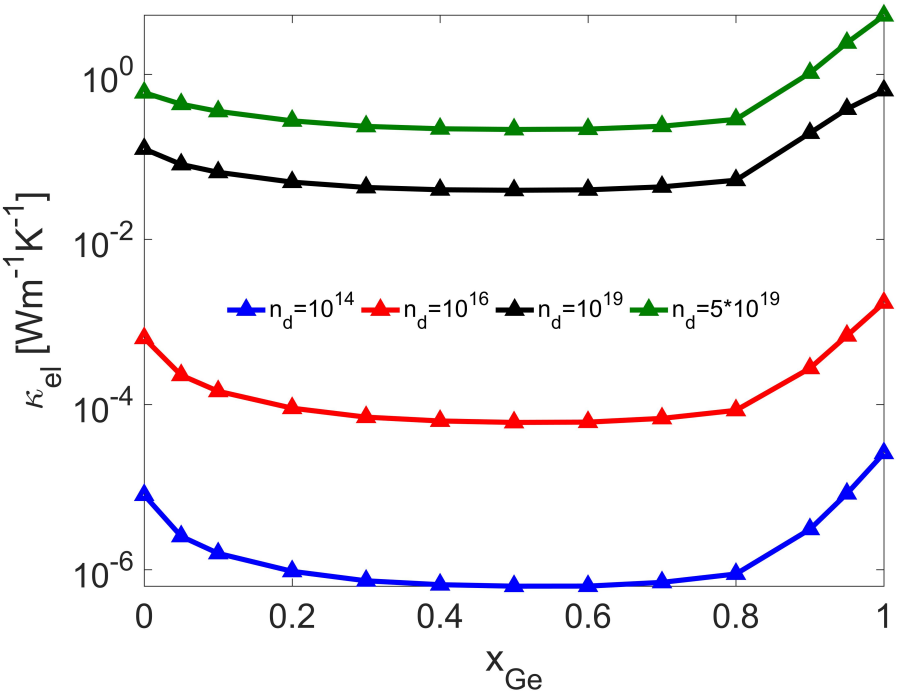

Figure 6.5. Electronic contribution to the thermal conductivity vs. Ge composition for four carrier concentrations of 10^{14},10^{16}, 10^{19} and 5×10^{19} cm^{-3}.

of thermal conductivity vs. Ge composition for donor concentrations of 10^{14},10^{16}, 10^{19} and 5×10^{19} cm^{-3}. This result illustrates that the significant thermal transport by electrons are occurring at high doping level, and κ_{ph} is weak for the low doping level, which in good agreement with [60].

6.2 Results and Discussions on ZT of Bulk and Nanostructure Alloys

Having all the electrical and thermal path parameters calculated, we are now in the position of calculating the ZT over a wide range of temperatures for both bulk and thin films. First, we calculate the ZT of bulk to find the optimal Ge compositions and carrier concentrations. Fig. 6.6 (a) depicts the ZT of bulk $Si_{1-x}Ge_x$ vs. the Ge composition for donor concentrations of 10^{14},10^{16}, 10^{19} and 5×10^{19} cm^{-3}. The

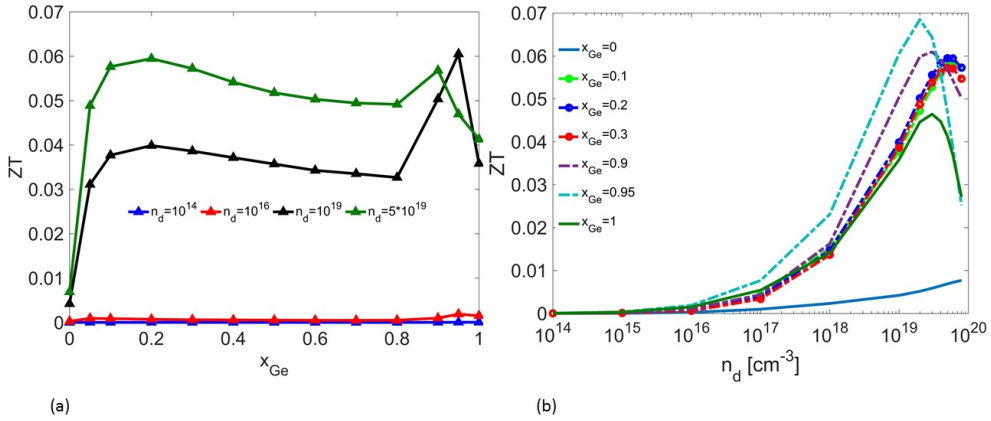

Figure 6.6. (a) ZT vs. x_{Ge} for n_d=10^{14}, 10^{16}, 10^{19} and 5×10^{19} cm^3. (b) ZT vs. n_d for Ge composition of $0, 0.1, 0.2, 0.3, 0.9, 0.95$, and 1.

trade-off between the increase of σ, decrease of S and increase of κ_{el} due to increasing the carrier concentrations, results in ZT to have its maximum in the range of 10^{19} and 10^{20} cm^{-3}. Higher carrier mobility and power factor of Ge compare to Si, result in higher power factor in the Ge side (x_{Ge}=0.9 and 0.95). This results in achieving higher ZT in these compositions. Besides, in the indirect band-gap semiconductors ZT peaks when the thermal energy is in the range of 6-10 k_BT [51]. Si has a bandgap of E_g=(1.21-4.1$\times10^{-4}$T) eV and Ge has a bandgap of E_g=(0.785-4.4$\times10^{-4}$T) eV [23]. Hence, in the lower temperatures, ZT of the alloy with higher Ge compositions peaks earlier. This effect is shown in Fig. 6.6 (b). On the other hand, the large bandgap of silicon ensures that in the alloys with higher Si compositions, minority carrier dominance does not arise. This gives us the possibility of increasing ZT values to 0.5 and higher by reducing thermal conductivity (because of increase in the phonon scattering) without affecting the electron mobility [11]. Having the range of the optimal compositions, we calculate the optimal carrier concentrations in which ZT peaks. Fig. 6.6 (b) shows the ZT vs. carrier concentrations for couple of Ge compositions that

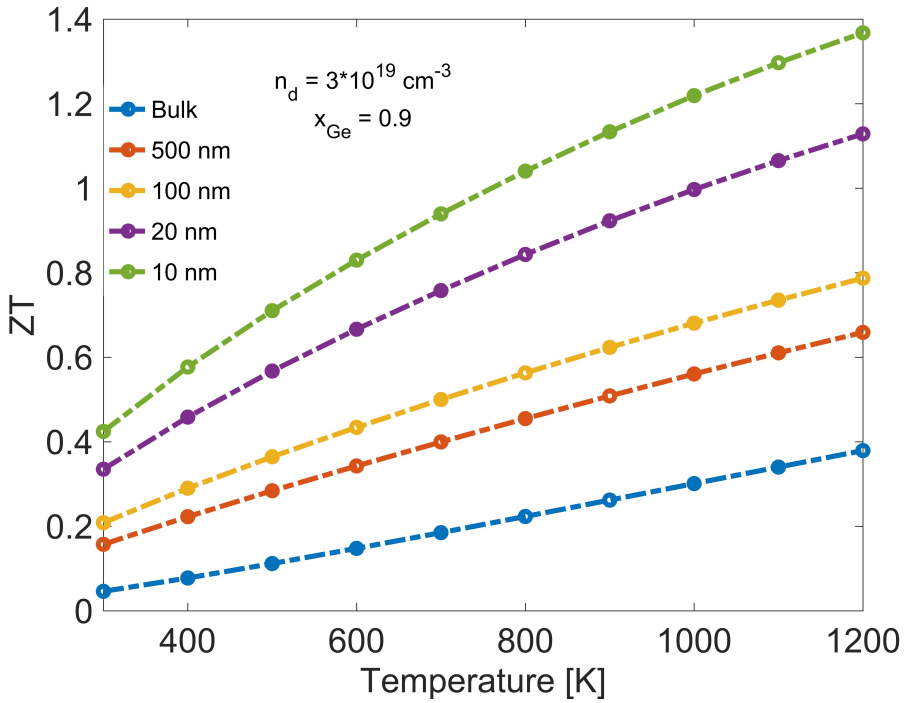

Figure 6.7. ZT vs. Temperature for Ge composition of 0.9 with n_d=3×10^{19} cm^{-3} for bulk, 500 nm, 100 nm, 20 nm and 10 nm.

that are more likely to produce the higher ZT. This plot illustrates that the alloys with higher Ge compositions peak earlier at lower carrier concentrations (x_{Ge}=0.95 at n_d=2×10^{19} cm^{-3} and x_{Ge}=0.90 at n_d=3×10^{19} cm^{-3}), while the alloys with lower Ge compositions peak later at higher carrier concentrations (x_{Ge}=0.1 at n_d=6×10^{19} cm^{-3} and x_{Ge}=0.2 at n_d=5×10^{19} cm^{-3}). Having the optimal alloy compositions and carrier concentrations, we are in the position of reducing the thermal conductivity by nanostructuring. The thin films that are studied in this thesis are range between 500 nm to 10 nm. The MFP of an electron is ten times lower than the lowest thin film. Hence, we can manipulate thermal path without significantly altering the electrical path. As a result, we calculated the ZT of four optimal compositions (0.1, 0.2, 0.9, and 0.95) each with the corresponding optimal carrier concentrations. The Fig. 6.7 and 6.8 depicts our results for higher Ge compositions and lower carrier concen-

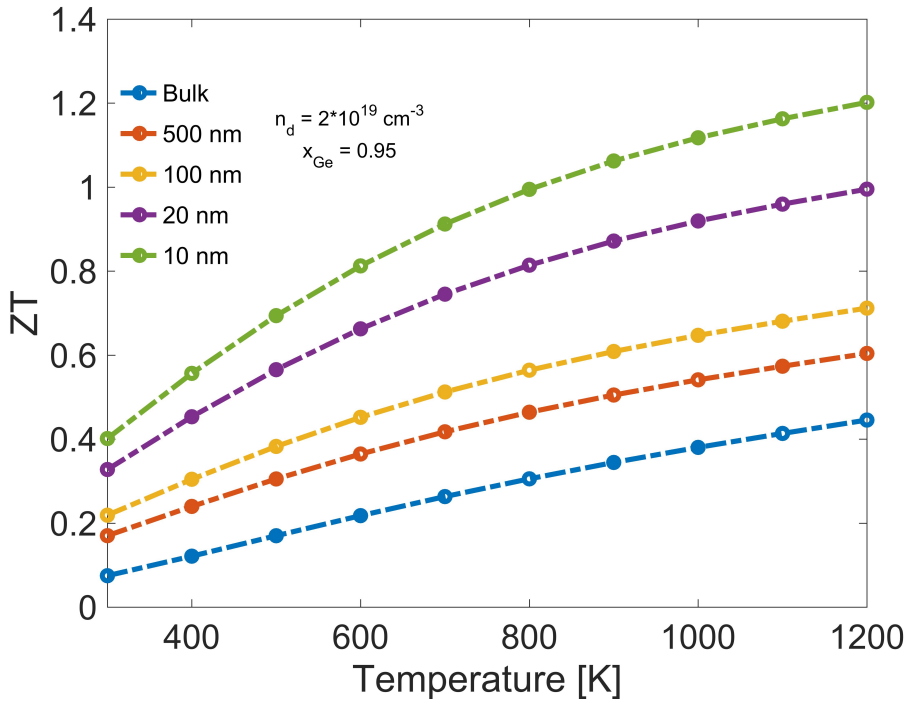

Figure 6.8. ZT vs. Temperature for Ge composition of 0.95 with n_d=2×10^{19} cm^{-3} for bulk, 500 nm, 100 nm, 20 nm and 10 nm.

trations and Fig. 6.9 and 6.10 demonstrates the results for lower Ge compositions at higher carrier concentrations. It is illustrated that tuning the thickness results in higher ZT, especially at the higher temperature. Our calculation shows that ZT reaches as high as 1.9 at the temperature of 1200 K and 1.58 at the temperature of 1000 K at Ge composition of 0.2 at 10 nm thickness with the carrier concentration of 5×10^{19} cm^{-3} (Fig. 6.10). Our model does not capture the thermal conductivity at higher temperatures, however, at very high temperatures, thermal conductivity starts to increase due to electron-hole pair creation and diffusion. At the high temperature, because of the large amount of available heat, electrons move toward the conduction band. Hence, electron-hole pairs are created. The electron-hole pair diffuse the temperature gradient down and will recombine again . During this process, an energy equals to the band gap releases [23]. Subsequently, thermal conductivity starts to

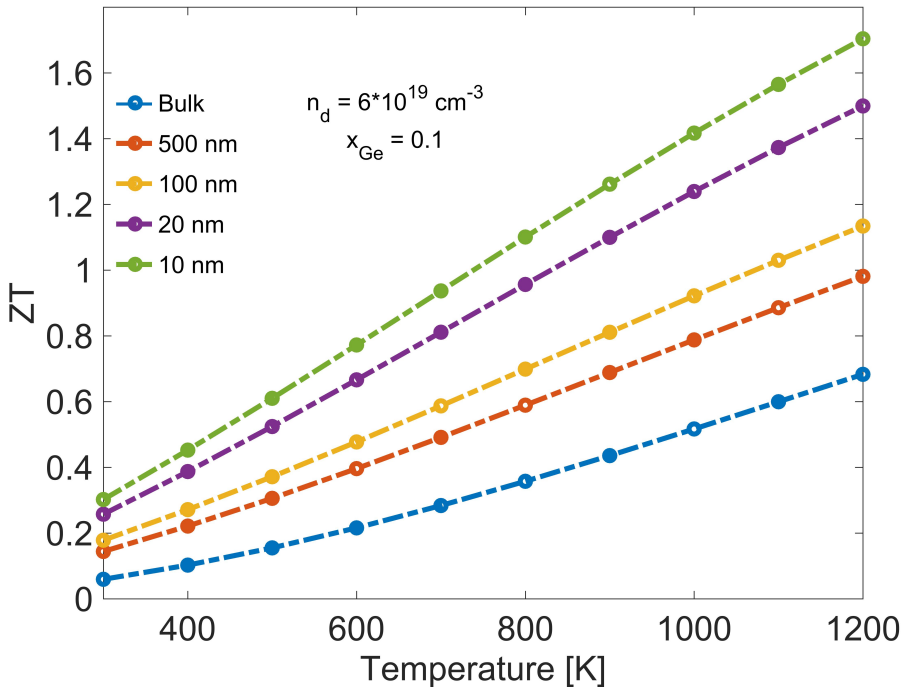

Figure 6.9. ZT vs. Temperature for Ge composition of 0.1 with n_d=6×10^{19} cm^{-3} for bulk, 500 nm, 100 nm, 20 nm and 10 nm.

increase resulting in the reduction of the ZT afterwards.

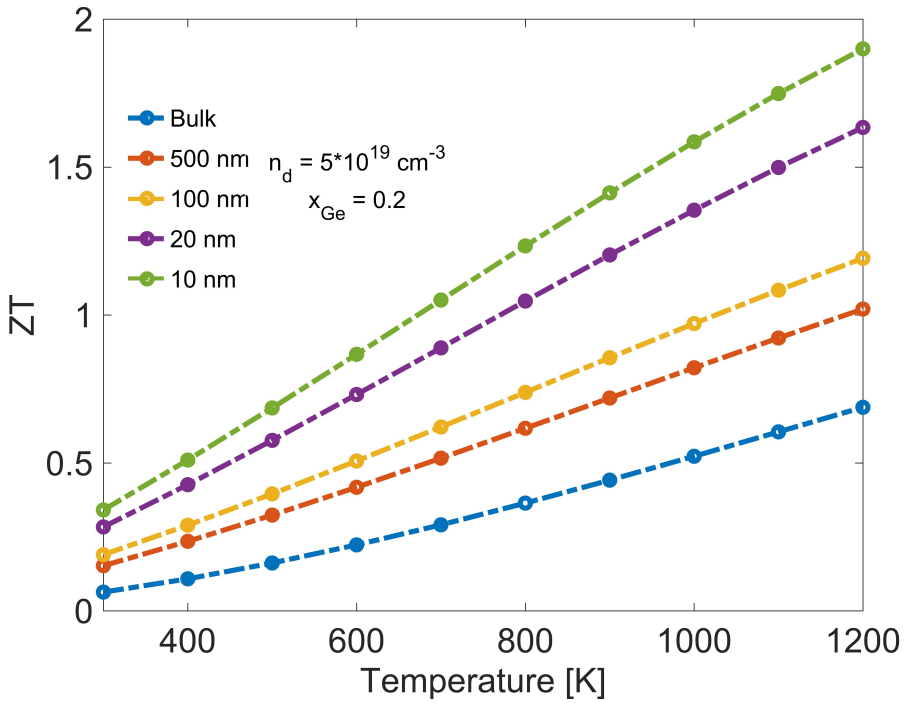

Figure 6.10. ZT vs. Temperature for Ge composition of 0.2 with n_d=5×10^{19} cm^{-3} for bulk, 500 nm, 100 nm, 20 nm and 10 nm.

CHAPTER 7

CONCLUSION

Si-based thermoelectric devices are widely used in nowadays technology. However, thermoelectric properties of materials are strongly correlated, this makes ZT improvement a challenging task. This study shows that nanostructuring and alloying can reduce κ_{ph} without significantly changing the other parameters. This is because of the phonon characteristics in solids in which MFP of phonons are much larger than those of electrons. This give us the possibility of phonon confinement without altering electron transport. In this study, thermal conductivity of group IV-based binary and ternary alloys such as SiGe, SiSn, GeSn, and SiGeSn were considered. Applying nanostructuring and alloying techniques, we reduced thermal conductivity of binary and ternary alloys. Our study shows that, due to the atomic mass difference, which gives rise to the elastic mass scattering mechanism as the most dominant one, SiSn has the lowest thermal conductivity among the other materials under study. SiSn achieved thermal conductivity of 1.18 W/mK at 10 nm at composition of 0.18, which is the experimentally stable state of SiSn. This value is lower than thermal conductivity of SiGe at 10 nm which is 1.43 W/mK. In the second part of this study, we considered the electronic transport of SiGe in order to see how much ZT improvement has been achieved using alloying and nanostructuring. We also studied the temperature dependence of thermal and electrical transport which implies that at higher temperature SiGe can achieve desired ZT. This model can be applied to SiSn and other binary ternary alloys, to calculate the improved ZT.

BIBLIOGRAPHY

[1] Abeles, B. Lattice thermal conductivity of disordered semiconductor alloys at high temperatures. *Phys. Rev. 131* (1963), 1906–1911.

[2] Abeles, B., Beers, D. S., Cody, G. D., and Dismukes, J. P. Thermal conductivity of ge-si alloys at high temperatures. *Phys. Rev. 125*, 1 (1962), 44–46.

[3] Adu, K. W., Gutierrez, H. R., Kim, U. J., Sumanasekera, G. U., and Eklund, P. C. Scaling laws of cumulative thermal conductivity for short and long phonon mean free paths. *Appl. Phys. Lett. 105*, 13 (2014), 131901.

[4] Aksamija, Z., and Knezevic, I. Anisotropy and boundary scattering in the lattice thermal conductivity of silicon nanomembranes. *Phys. Rev. B 82* (2010), 045319.

[5] Aksamija, Z., and Knezevic, I. Thermoelectric properties of silicon nanostructures. *J. Comput. Electron. 9* (2010), 173.

[6] Aksamija, Z., and Knezevic, I. Thermal conductivity of $Si_{1-x}Ge_x/Si_{1-y}Ge_y$ superlattices: Competition between interfacial and internal scattering. *Phys. Rev. B 88* (2013), 155318.

[7] Aksamija, Z., and Ravaioli, U. Anharmonic decay of g-process longitudinal optical phonons in silicon. *Appl. Phys. Lett. 96*, 9 (2010), 091911.

[8] Amith, A. Seebeck coefficient in N-type germanium-silicon alloys: "competition" region. *Physical Review 139*, 5A (1965), A1624.

[9] Bauer, Matthew, Ritter, Cole, Crozier, P. A., Ren, Jie, Menendez, J., Wolf, G., and Kouvetakis, J. Synthesis of ternary sigesn semiconductors on Si(100) via Sn_xGe_{1-x} buffer layers. *Appl. Phys. Lett. 83*, 11 (2003), 2163–2165.

[10] Bera, Chandan, Soulier, M., Navone, C., Roux, Guilhem, Simon, J., Volz, S., and Mingo, Natalio. Thermoelectric properties of nanostructured $Si_{1-x}Ge_x$ and potential for further improvement. *J. Appl. Phys. 108*, 12 (2010), 124306.

[11] Bulusu, A., and Walker, D.G. Review of electronic transport models for thermoelectric materials. *Superlatt. Microstruct. 44* (2008), 1–36.

[12] Cahill, David G., Watson, S. K., and Pohl, R. O. Lower limit to the thermal conductivity of disordered crystals. *Phys. Rev. B 46*, 10 (1992), 6131–6140.

[13] Carruthers, Peter. Theory of thermal conductivity of solids at low temperatures. *Rev. Mod. Phys. 33*, 1 (1961), 92.

[14] Cheaito, Ramez, Duda, John C., Beechem, Thomas E., Hattar, Khalid, Ihlefeld, Jon F., Medlin, Douglas L., Rodriguez, Mark A., Campion, Michael J., Piekos, Edward S., and Hopkins, Patrick E. Experimental investigation of size effects on the thermal conductivity of silicon-germanium alloy thin films. *Phys. Rev. Lett. 109* (2012), 195901.

[15] Chen, Gang. *Nanoscale energy transport and conversion.* Oxford University Press, New York, 2005.

[16] D'Costa, V. R., Fang, Y.-Y., Tolle, J., Kouvetakis, J., and Menéndez, J. Tunable optical gap at a fixed lattice constant in group-iv semiconductor alloys. *Phys. Rev. Lett. 102* (2009), 107403.

[17] DiSalvo, F. J. Thermoelectric cooling and power generation. *Science 285* (1999), 703–706.

[18] Dresselhaus, M. S., Chen, G., Tang, M. Y., Yang, R. G., Lee, H., Wang, D. Z., Ren, Z. F., Fleurial, J.-P., and Gogna, P. New directions for low-dimensional thermoelectric materials. *Adv. Mater. 19* (2007), 1043–1053.

[19] Feser, Joseph P., Chan, Emory M., Majumdar, Arun, Segalman, Rachel A., and Urban, Jeffrey J. Ultralow thermal conductivity in polycrystalline CdSe thin films with controlled grain size. *Nano Lett. 13*, 5 (2013), 2122–2127.

[20] Frachioni, Anthony, and White, B. E. Simulated thermal conductivity of silicon-based random multilayer thin films. *J. Appl. Phys. 112*, 1 (2012).

[21] Garg, Jivtesh, Bonini, Nicola, Kozinsky, Boris, and Marzari, Nicola. Role of disorder and anharmonicity in the thermal conductivity of silicon-germanium alloys: A first-principles study. *Phys. Rev. Lett. 106* (2011), 045901.

[22] Gilat, G., and Raubenheimer, L. J. Accurate numerical method for calculating frequency-distribution functions in solids. *Phys. Rev. 144*, 2 (1966), 390–395.

[23] Glassbrenner, C. J., and Slack, Glen A. Thermal conductivity of silicon and germanium from 3 K to the melting point. *Phys. Rev. 134*, 4A (1964), A1058–A1069.

[24] Hicks, L. D., and Dresselhaus, M. S. Effect of quantum-well structures on the thermoelectric figure of merit. *Phys. Rev. B 47* (1993), 12727.

[25] Hicks, L.D., and Dresselhaus, M.S. Thermoelectric figure of merit of a one-dimensional conductor. *Phys. Rev. B 47* (1993), 16631.

[26] Joshi, Giri, Lee, Hohyun, Lan, Yucheng, Wang, Xiaowei, Zhu, Gaohua, Wang, Dezhi, Gould, Ryan W., Cuff, Diana C., Tang, Ming Y., Dresselhaus, Mildred S., Chen, Gang, and Ren, Zhifeng. Enhanced thermoelectric figure-of-merit in nanostructured p-type silicon germanium bulk alloys. *Nano Lett. 8*, 12 (2008), 4670–4674.

[27] Khatami, SN, and Aksamija, Z. Lattice thermal conductivity of the binary and ternary group-iv alloys si-sn, ge-sn, and si-ge-sn. *Physical Review Applied 6*, 1 (2016), 014015.

[28] Klemens, P.G. *Solid state physics*. Academic Press, NY, 1958.

[29] Kurosawa, Masashi, Kato, Motohiro, Yamaha, Takashi, Taoka, Noriyuki, Nakatsuka, Osamu, and Zaima, Shigeaki. Near-infrared light absorption by polycrystalline SiSn alloys grown on insulating layers. *Appl. Phys. Lett. 106*, 17 (2015).

[30] Lee, Jaeho, Lim, Jongwoo, and Yang, Peidong. Ballistic phonon transport in holey silicon. *Nano Letters 15*, 5 (2015), 3273–3279.

[31] Liao, C. N., Chen, C., and Tu, K. N. Thermoelectric characterization of Si thin films in silicon-on-insulator wafers. *J. Appl. Phys. 86*, 6 (1999), 3204–3208.

[32] Liu, Wenjun, and Asheghi, Mehdi. Thermal conduction in ultrathin pure and doped single-crystal silicon layers at high temperatures. *J. Appl. Phys. 98*, 12 (2005), 123523.

[33] Maris, Humphrey J. Phonon propagation with isotope scattering and spontaneous anharmonic decay. *Phys. Rev. B 41*, 14 (1990), 9736–9743.

[34] Martin, Pierre, Aksamija, Zlatan, Pop, Eric, and Ravaioli, Umberto. Impact of phonon-surface roughness scattering on thermal conductivity of thin Si nanowires. *Phys. Rev. Lett. 102*, 12 (2009), 125503.

[35] Maycock, P.D. Thermal conductivity of silicon, germanium, iii-v compounds and iii-v alloys. 161 – 168.

[36] Mehrotra, Saumitra R, Paul, Abhijeet, and Klimeck, Gerhard. Atomistic approach to alloy scattering in $Si_{1-x}Ge_x$. *Applied Physics Letters 98*, 17 (2011), 173503.

[37] Minnich, A. J., Lee, H., Wang, X. W., Joshi, G., Dresselhaus, M. S., Ren, Z. F., Chen, G., and Vashaee, D. Modeling study of thermoelectric SiGe nanocomposites. *Phys. Rev. B 80*, 15 (2009), 155327.

[38] Morelli, D. T., Heremans, J. P., and Slack, G. A. Estimation of the isotope effect on the lattice thermal conductivity of group IV and group III-V semiconductors. *Phys. Rev. B 66*, 19 (2002), 195304.

[39] Mupadhyaya, M., Khatami, S. N., and Aksamija, Z. Engineering thermal transport in sige-based nanostructures for thermoelectric applications. *J. Mat. Research 30* (2015), 2649–2662.

[40] Murphy-Armando, F., and Fahy, S. First-principles calculation of carrier-phonon scattering in n-type si1−xgex alloys. *Phys. Rev. B 78* (2008), 035202.

[41] Price, D. L., Rowe, J. M., and Nicklow, R. M. Lattice dynamics of grey tin and indium antimonide. *Phys. Rev. B 3* (1971), 1268–1279.

[42] Rajput, B. D., and Browne, D. A. Lattice dynamics of ii-vi materials using the adiabatic bond-charge model. *Phys. Rev. B 53*, 14 (1996), 9052–9058.

[43] Ridley, Brian K. *Quantum processes in semiconductors*. Oxford University Press, 2013.

[44] Rieger, Martin M., and Vogl, P. Electronic-band parameters in strained $si_{1-x}ge_x$ alloys on $si_{1-y}ge_y$ substrates. *Phys. Rev. B 48*, 19 (1993), 14276–14287.

[45] Rode, D. L. Electron transport in insb, inas, and inp. *Phys. Rev. B 3* (1971), 3287–3299.

[46] Rustagi, K. C., and Weber, W. Adiabatic bond charge model for the phonons in a3b5 semiconductors. *Solid State Comm. 18*, 6 (1976), 673 – 675.

[47] Ryu, H. J., Aksamija, Z., Paskiewicz, D. M., Scott, S. A., Lagally, M. G., Knezevic, I., and Eriksson, M. A. Quantitative determination of contributions to the thermoelectric power factor in si nanostructures. *Phys. Rev. Lett. 105* (2010), 256601.

[48] Slack, G. *Solid State Physics, vol. 34*. Academic Press, New York, NY, 1979.

[49] Snyder, G. Jeffrey, and Toberer, Eric S. Complex thermoelectric materials. *Nature Mater. 7*, 2 (2008), 105–114.

[50] Snyder, G. Jeffrey, Toberer Eric S. Complex thermoelectric materials. *Nature*.

[51] Sofo, JO, and Mahan, GD. Optimum band gap of a thermoelectric material. *Physical Review B 49*, 7 (1994), 4565.

[52] Sondheimer, E. H. The mean free path of electrons in metals. *Adv. Phys. 1* (1952), 1–42.

[53] Strauch, D., and Dorner, B. Phonon dispersion in GaAs. *J. Phys.: Condens. Matter 2* (1990), 1457–1474.

[54] Tamura, Shin-Ichiro. Isotope scattering of dispersive phonons in Ge. *Phys. Rev. B 27*, 2 (1983), 858–866.

[55] Tonkikh, A.A., Zakharov, N.D., Eisenschmidt, C., Leipner, H.S., and Werner, P. Aperiodic sisn/si multilayers for thermoelectric applications. 49 – 51.

[56] Turney, J. E., McGaughey, A. J. H., and Amon, C. H. In-plane phonon transport in thin films. *J. Appl. Phys. 107*, 2 (2010), 024317.

[57] Vasileska, Dragica, Goodnick, Stephen M, and Klimeck, Gerhard. *Computational electronics: semiclassical and quantum device modelling and simulation.* CRC Press, New York, 2012.

[58] Vineis, C. J, Shakouri, A., Majumdar, A., and Kanatzidis, M. G. Nanostructured thermoelectrics: Big efficiency gains from small features. *Adv. Mater. 22*, 36 (2010), 3970–3980.

[59] Vining, Cronin B. An inconvenient truth about thermoelectrics. *Nat Mater 8*, 2 (2009), 83–85.

[60] Wang, Zhao, Wang, Shidong, Obukhov, Sergey, Vast, Nathalie, Sjakste, Jelena, Tyuterev, Valery, and Mingo, Natalio. Thermoelectric transport properties of silicon: Toward an *ab initio* approach. *Phys. Rev. B 83* (2011), 205208.

[61] Weber, W. Adiabatic bond charge model for the phonons in diamond, si, ge, and a-sn. *Phys. Rev. B 15*, 10 (1977), 4789.

[62] Zebarjadi, M., Esfarjani, K., Dresselhaus, M. S., Ren, Z. F., and Chen, G. Perspectives on thermoelectrics: from fundamentals to device applications. *Energy Environ. Sci. 5* (2012), 5147–5162.

[63] Zhu, G. H., Lee, H., Lan, Y. C., Wang, X. W., Joshi, G., Wang, D. Z., Yang, J., Vashaee, D., Guilbert, H., Pillitteri, A., Dresselhaus, M. S., Chen, G., and Ren, Z. F. Increased phonon scattering by nanograins and point defects in nanostructured silicon with a low concentration of germanium. *Phys. Rev. Lett. 102*, 19 (May 2009), 196803.